ATLAS NOTE

ATLAS-CONF-2013-065

July 12, 2013

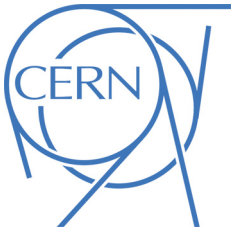

Searches for direct scalar top pair production in final states with two leptons using the stransverse mass variable and a multivariate analysis technique in $\sqrt{s} = 8$ TeV pp collisions using 20.3 fb^{-1} of ATLAS data

The ATLAS Collaboration

ATLAS-CONF-2013-065
18 July 2013

Abstract

Two searches are presented for the direct pair production of supersymmetric partners of the top quark in 20.3 fb^{-1} of pp collisions at $\sqrt{s} = 8$ TeV, collected by the ATLAS detector at the LHC. Top squarks are sought for in events with two leptons (e or μ) in the final state. No excess above the Standard Model expectation is observed. Exclusion limits at 95% confidence level are derived on the mass of the top squark assuming it decays with 100% branching ratio into a b-quark and a chargino, using a search which exploits the stransverse mass variable, or into a top quark and the lightest neutralino using a multivariate analysis technique.

1 Introduction

Partners of the top quark are a key ingredient in several theories addressing the hierarchy problem [1–4] of the Standard Model (SM). In order to stabilise the Higgs boson mass against quadratically divergent quantum corrections, these new particles should have masses close to the electroweak symmetry breaking energy scale, and thus be accessible at the LHC [5]. One of these theories is supersymmetry (SUSY) [6–14] which naturally resolves the hierarchy problem by introducing supersymmetric partners of the known bosons and fermions. In the R-parity conserving minimal supersymmetric extension of the SM (MSSM) [15–19] the scalar partners of right-handed and left-handed quarks can mix to form two mass eigenstates, $\tilde{q}_1$ and $\tilde{q}_2$, with $\tilde{q}_1$ defined to be the lighter one. In the case of the supersymmetric partner of the top quark ($\tilde{t}$, stop), the large top Yukawa coupling affects both off- and on-diagonal terms of the mass matrix, leading to one stop mass eigenstate, $\tilde{t}_1$, that is significantly lighter than the other squarks.

The stop can decay into a variety of final states, depending, amongst other factors, on the mass hierarchy of the lightest chargino ($\tilde{\chi}_1^\pm$) and the lightest neutralino ($\tilde{\chi}_1^0$). Two decay modes are considered separately in this note, each assumed to have 100% branching ratio (BR): $\tilde{t}_1 \to b + \tilde{\chi}_1^\pm$, and $\tilde{t}_1 \to t + \tilde{\chi}_1^0$. The first decay mode requires $m(\tilde{t}_1) - m(\tilde{\chi}_1^\pm) > m(b)$, the $\tilde{\chi}_1^\pm$ subsequently decaying into the lightest neutralino (assumed to be the lightest supersymmetric particle (LSP) and stable), and a real or virtual W boson. In the second decay mode only on-shell top quarks are considered, limiting the analysis to a stop heavier than the top quark and the lightest neutralino. In both cases the stops are pair produced and since we consider only the leptonic decay mode of the $W^{(*)}$, the events are characterised by the presence of two isolated leptons (e, μ) with opposite charge, and two b-quarks. Significant transverse momentum $\mathbf{p}_\mathrm{T}^\mathrm{miss}$, whose magnitude is referred to as $E_\mathrm{T}^\mathrm{miss}$, is also expected from the neutrinos and neutralinos in the final states.

The first search, denoted $b + \tilde{\chi}_1^\pm$ in the following, is designed to complement the analysis in Ref. [20] which searches for this decay using the stransverse mass [21, 22]. This quantity is defined as:

$$m_\mathrm{T2}(\mathbf{p}_\mathrm{T}^1, \mathbf{p}_\mathrm{T}^2, \mathbf{q}_\mathrm{T}) = \min_{\mathbf{q}_\mathrm{T}^1 + \mathbf{q}_\mathrm{T}^2 = \mathbf{q}_\mathrm{T}} \left\{ \max[\, m_\mathrm{T}(\mathbf{p}_\mathrm{T}^1, \mathbf{q}_\mathrm{T}^1), m_\mathrm{T}(\mathbf{p}_\mathrm{T}^2, \mathbf{q}_\mathrm{T}^2)\,] \right\}, \tag{1}$$

where m_T indicates the transverse mass[1], $\mathbf{p}_\mathrm{T}^1$ and $\mathbf{p}_\mathrm{T}^2$ are the transverse momenta of two particles (assumed to be massless), and $\mathbf{q}_\mathrm{T}^1$ and $\mathbf{q}_\mathrm{T}^2$ are vectors which satisfy $\mathbf{q}_\mathrm{T}^1 + \mathbf{q}_\mathrm{T}^2 = \mathbf{q}_\mathrm{T}$. The minimisation is performed over all the possible decompositions of $\mathbf{q}_\mathrm{T}$. For top quark and W boson pair decay, if the transverse momenta of the two leptons in each event are taken as $\mathbf{p}_\mathrm{T}^1$ and $\mathbf{p}_\mathrm{T}^2$ respectively and $E_\mathrm{T}^\mathrm{miss}$ as $\mathbf{q}_\mathrm{T}$, $m_\mathrm{T2}(\ell, \ell, E_\mathrm{T}^\mathrm{miss})$ is bound sharply from above by the mass of the W [23, 24]. In the stop decay considered the bound is strongly correlated with the mass difference between the chargino and the lightest neutralino. In [20] these different bounds are exploited to search with good sensitivity for the $b + \tilde{\chi}_1^\pm$ decay mode for models with mass difference between the chargino and the lightest neutralino greater than the value of the W boson mass. The search presented in this note aims to have sensitivity to models with smaller chargino-neutralino mass differences. The stransverse mass is employed as follows: the transverse momenta of the two reconstructed b-quarks in the event are taken as $\mathbf{p}_\mathrm{T}^1$ and $\mathbf{p}_\mathrm{T}^2$, and the lepton transverse momenta are added vectorially to the missing transverse momentum in the event to form $\mathbf{q}_\mathrm{T}$. The resulting $m_\mathrm{T2}(b, b, \ell + \ell + E_\mathrm{T}^\mathrm{miss})$ has a very different kinematic limit than before: for top pair production it is approximately bound by the mass of the top, whilst for stop decays the bound is strongly correlated to the mass difference between the stop and the chargino. A high cut on this variable is thus sensitive to large stop-chargino mass differences and small chargino-neutralino mass differences. In this note the $m_\mathrm{T2}(\ell, \ell, E_\mathrm{T}^\mathrm{miss})$ is referred to simply as m_T2, whilst $m_\mathrm{T2}(b, b, \ell + \ell + E_\mathrm{T}^\mathrm{miss})$ is referred to as $m_\mathrm{T2}^\text{b-jet}$.

[1] $m_\mathrm{T} = \sqrt{2|\mathbf{p}_\mathrm{T}^1||\mathbf{p}_\mathrm{T}^2|(1 - \cos(\phi))}$ where ϕ is the angle between the particles with transverse momenta $\mathbf{p}_\mathrm{T}^1$ and $\mathbf{p}_\mathrm{T}^2$ in the transverse plane.

The results of this search are interpreted in a two-dimensional plane of varying chargino and the lightest neutralino masses for a stop mass of 300 GeV, following Ref. [20].

The m_{T2} observable is also a valuable discriminant for the search of a stop decaying into a top and the lightest neutralino, which represents the second search of this note, denoted $t + \tilde{\chi}_1^0$ in the following. In this search signal events are separated from SM backgrounds using a multivariate analysis (MVA) technique based on boosted decision trees (BDT) and applying a gradient boosting algorithm (BDTG) [25]. Discriminating variables which exploit several geometric and kinematic features of the stop decays are used as input to the BDTG, the m_{T2} variable being one of the most effective inputs. This search utilises the TMVA toolkit for multivariate data analysis [26]. The results are interpreted in a two-dimensional plane of varying stop and lightest neutralino masses.

Previous ATLAS analyses using 2011 ATLAS data have placed exclusions on both the $\tilde{t}_1 \rightarrow b + \tilde{\chi}_1^{\pm}$ [27, 28] and $\tilde{t}_1 \rightarrow t + \tilde{\chi}_1^0$ [29–31] decay modes. Preliminary analyses of 2012 ATLAS and CMS data have placed further constraints on these decay modes [20, 32–38].

2 The ATLAS detector

ATLAS is a multi-purpose particle physics experiment at the LHC. The detector layout [39] consists of inner tracking devices surrounded by a superconducting solenoid, electromagnetic and hadronic calorimeters and a muon spectrometer immersed in a toroidal magnetic field. The inner detector, in combination with the axial 2 T field from the solenoid, provides precision tracking of charged particles for $|\eta| < 2.5$[2]. It consists of a silicon pixel detector, a silicon strip detector and a straw tube tracker that also provides transition radiation measurements for electron identification. The calorimeter system covers the pseudorapidity range $|\eta| < 4.9$. In the region $|\eta| < 3.2$ high granularity liquid argon electromagnetic sampling calorimeters are used. An steel/scintillator-tile calorimeter provides energy measurement for hadrons in $|\eta| < 1.7$. The end-cap and forward regions, which span $1.5 < |\eta| < 4.9$, are instrumented with liquid argon calorimetry for both electromagnetic and hadronic particles. The muon spectrometer has separate trigger and high-precision tracking chambers which provide muon trigger and measurement capabilities for $|\eta| < 2.4$ and $|\eta| < 2.7$ respectively.

3 Monte Carlo simulation

Monte Carlo (MC) simulated event samples are used to model the signal and to describe all the backgrounds which produce events with two prompt leptons. For top quark pair production (and additionally Z/γ^*+jets in the $b + \tilde{\chi}_1^{\pm}$ analysis) the shape of the kinematic distributions are taken from MC simulation, while the normalisation is determined by measurements in appropriate control regions as described in Section 6. The remaining backgrounds which produce two prompt leptons are evaluated using simulations only. The contribution from events containing leptons from heavy flavour decays or jet(s) misidentified as leptons is estimated from data. This class of event is referred to as "fake lepton" in what follows.

Top-quark pair and Wt production are simulated with `MC@NLO` [40, 41], interfaced with `Herwig` [42] for the fragmentation and the hadronisation processes, including `Jimmy` [43] for the underlying event description. Additional `AcerMC` [44] samples and `PowHeg` [45] samples, interfaced to both `Pythia` [46] and `Herwig`, are used to estimate the event generator, fragmentation and hadronisation systematic uncertainties.

Samples of $t\bar{t}Z$ and $t\bar{t}W$ production are generated with `MadGraph` [47] interfaced to `Pythia`.

[2] ATLAS uses a right-handed coordinate system with its origin at the nominal interaction point (IP) in the centre of the detector and the z-axis coinciding with the axis of the beam pipe. The x-axis points from the IP to the centre of the LHC ring, and the y-axis points upwards. Cylindrical coordinates (r, ϕ) are used in the transverse plane, ϕ being the azimuthal angle around the beam pipe. The pseudorapidity is defined in terms of the polar angle θ as $\eta = -\ln\tan(\theta/2)$.

Table 1: The leading SM background processes and their production cross sections. For $t\bar{t}$ and $Z/\gamma^\star$, the production cross section is multiplied by the branching ratio of the leptonic decays indicated in the first column, where $\ell = e, \mu$, or τ. The last two columns give the perturbative order of the calculation and the relevant reference.

Physics process	σ [pb]	Perturbative order in α_s	Reference
$Z/\gamma^\star \to \ell\ell, m(\ell\ell) > 40$ GeV	1240 ± 60	DYNNLO	[52]
$t\bar{t} \to \ell + X$	129^{+12}_{-13}	NLO+NNLL	[54]
Wt	22.4 ± 1.5	NLO+NNLL	[55]
$t\bar{t}W$	0.23 ± 0.07	NLO	[57]
$t\bar{t}Z$	0.21 ± 0.06	NLO	[57]
WW	54.7 ± 3.3	NLO	[40, 56]
WZ	33.3 ± 1.7	NLO	[40, 56]
ZZ	11.2 ± 0.8	NLO	[40, 56]

Samples of $Z/\gamma^\star$ produced in association with jets are generated with `Sherpa` [48] using the PDF set CT10 [49], while `Alpgen` [50] samples, using the PDF set CTEQ6.1 [51], are considered for systematics evaluation.

Diboson samples (WW, WZ, ZZ) are generated with `PowHeg` using the PDF set CT10. Additional samples generated with `Sherpa` are used to estimate the event generator systematic uncertainties.

The background predictions are normalised to the theoretical cross-sections, including higher-order QCD corrections where available, and are compared to data in dedicated control regions. The inclusive cross section for Z/γ^*+jets is calculated with DYNNLO [52] with the MSTW 2008 NNLO PDF [53]. Approximate NLO+NNLL (next-to-next-to-leading-logarithm) cross sections are used for the normalisation of the $t\bar{t}$ [54] and Wt [55] samples. NLO cross sections are used for the diboson samples [40, 56] and for the $t\bar{t}W$ and $t\bar{t}Z$ [57] samples. Table 1 summarises the production cross sections used in these analyses and their uncertainties.

The following processes producing two charged leptons in the final state have been considered and found to be negligible: Higgs production and decay into boson pairs, dilepton pairs produced via Drell-Yan processes with invariant mass < 40 GeV and production of $t\bar{t}$ WW final states.

Stop signal samples for the $b + \tilde{\chi}_1^\pm$ decay mode are generated with `MadGraph` interfaced to `Pythia` for a fixed 300 GeV stop mass, lightest neutralino mass values between 0 and 200 GeV and chargino mass values between 100 and 290 GeV. The 300 GeV stop is forced to decay exclusively into a b-quark and a $\tilde{\chi}_1^\pm$. Signal samples for the $t + \tilde{\chi}_1^0$ decay mode are generated with `Herwig++` [58]. The stop is forced to decay exclusively into a t-quark and a $\tilde{\chi}_1^0$. The mass of the stop is varied between 200 and 600 GeV, whilst the mass of the lightest neutralino varies from 0 to 400 GeV. Signal cross sections are calculated to NLO in the strong coupling constant, including the resummation of soft gluon emission at next-to-leading-logarithmic accuracy (NLO+NLL) [59–61], as described in Ref. [62].

All MC generator parameters have been tuned to ATLAS data [63, 64] and generated events are passed through a `GEANT4` [65] based detector simulation [66]. The $t\bar{t}$ from `PowHeg`, Z/γ^*+jets from `Sherpa`, all `AcerMC` samples and the stop signal samples are not reconstructed with the full detector simulation. Instead they are passed through the fast detector simulation `AtlFast-II` [67]. Effects of multiple proton-proton interactions in the same bunch crossing (pile-up) are included, and the MC simulated samples are re-weighted in such a way that the distribution of the average number of interactions per bunch crossing matches that in the data.

4 Event reconstruction

Proton-proton interaction vertex candidates are reconstructed using the tracks in the inner detector. The vertex with the highest scalar sum of the p_{T}^2 of the associated tracks is defined as the primary vertex.

Jets are reconstructed from three-dimensional energy clusters in the calorimeter using the anti-k_t jet clustering algorithm [68, 69] with a radius parameter of 0.4. The cluster energy is corrected using calibration factors based on MC simulation and validated with extensive test-beam and collision-data studies [70], in order to take into account effects such as non-compensation and inhomogeneities, the presence of dead material and out-of-cluster energy deposits. Corrections for jet energy scale and for in-time and out-of-time pile-up are also applied, as described in Ref. [71]. Only jet candidates with $p_{\mathrm{T}} > 20$ GeV, $|\eta| < 2.5$ and a "jet vertex fraction" larger than 0.5, for those with $p_{\mathrm{T}} < 50$ GeV, are considered as selected jets in the analysis. The jet vertex fraction quantifies the fraction of the jet track momentum that originates from the reconstructed primary vertex. This requirement rejects jets originating from additional proton-proton interactions occurring in the same bunch crossing. Events containing jets that are likely to have arisen from detector noise or cosmic rays are removed [72].

A neural-network-based algorithm is used to identify which of the selected jet candidates contain a b-hadron decay (b-jets). This uses as input the weights returned by various algorithms which exploit the impact parameters of inner detector tracks, secondary vertex reconstruction and the topology of weak b- and c-hadron decays inside a jet [73]. The efficiency for tagging b-jets in a MC sample of $t\bar{t}$ events using this algorithm is 70% with rejection factors of 137, 5 and 13 against light quarks, c-quarks and τ leptons respectively. To compensate for differences between the b-tagging efficiencies and mis-tag rates in data and MC simulation, scale factors are applied to the jets in the simulation as described in Ref. [74].

Electron candidates are required to have $p_{\mathrm{T}} > 20$ GeV, $|\eta| < 2.47$ and to satisfy "medium" electromagnetic shower shape and track selection quality criteria [75]. Signal electrons are then required to pass "tight" quality criteria, as desribed in the reference above. They are also required to be isolated within the tracking volume: the scalar sum, Σp_{T}, of the p_{T} of inner detector tracks with $p_{\mathrm{T}} > 1$ GeV, not including the electron track, within a cone in the $\eta - \phi$ plane of radius $\Delta R = \sqrt{\Delta\eta^2 + \Delta\phi^2} = 0.2$ around the electron candidate must be less than 10% of the electron p_{T}, where $\Delta\eta$ and $\Delta\phi$ are separations in η and ϕ.

Muon candidates are reconstructed using either a full muon spectrometer track matched to an inner detector track, or a muon spectrometer segment matched to an extrapolated inner detector track [76]. They must have sufficient hits in the pixel, strip and straw tube detectors and are required to have $p_{\mathrm{T}} > 10$ GeV and $|\eta| < 2.4$. Their longitudinal and transverse impact parameters must be within 1 mm and 0.2 mm of the primary vertex, respectively. Such preselected candidates are then required to have $\Sigma p_{\mathrm{T}} < 1.8$ GeV, where Σp_{T} is defined in analogy to the electron case.

Overlaps between jet, electron and muon candidates are defined in terms of ΔR. They are resolved as follows: any jet within $\Delta R = 0.2$ of preselected electrons is discarded; electrons or muons within $\Delta R = 0.4$ of any remaining jet are then ignored to reject leptons from the decay of a b- or c-hadron.

The magnitude of the two-vector obtained from the negative vector sum of the transverse momenta of all reconstructed electrons, jets and muons and calorimeter energy clusters not associated with any objects is conventionally denoted as $E_{\mathrm{T}}^{\mathrm{miss}}$. Clusters associated with either electrons or photons with $p_{\mathrm{T}} > 10$ GeV, and those associated with jets with $p_{\mathrm{T}} > 20$ GeV make use of the calibrations of these respective objects. For jets the calibration includes the pile-up correction described above and the jet vertex fraction requirement is not considered when selecting jet candidates. Calorimeter clusters with $|\eta| < 4.9$ not associated to these objects are calibrated using both calorimeter and tracker information [77].

5 Event selection

5.1 Preselection

The searches presented use proton-proton collisions recorded at a centre-of-mass energy of 8 TeV. Data were collected based on the decision of a three-level trigger system. Events are accepted if they passed either a single-electron, a single-muon, a double-electron, a double-muon, or an electron-muon trigger. The trigger efficiency exceeds 99% for the events passing the full selection described below. After beam, detector and data quality requirements, data corresponding to a total integrated luminosity of 20.3 fb^{-1} are used [78].

Events are required to have exactly two opposite-sign (OS) leptons (electrons, muons or one of each). At least one of the seleted electrons or muons must have transverse momentum (p_{T}) greater than 25 GeV, in order for the event to be triggered with high efficiency, and the invariant mass of the two leptons (m_{ll}) is required to be larger than 20 GeV. If the event contains a third preselected electron or muon, the event is rejected.

5.2 Event selection in the $b + \tilde{\chi}_1^{\pm}$ analysis

Further to the preselection described in Section 5.1, events are required to have exactly 2 b-jets, $m_{\text{T2}}^{\text{b-jet}} >$ 160 GeV, $m_{\text{T2}} < 90$ GeV and leading lepton $p_{\text{T}} < 60$ GeV. The 2 b-jet requirement strongly favours signal over background, reducing the latter after pre-selection by a factor of ∼300 whilst reducing the yields of the key signal points by at most factors of ∼10. The $t\bar{t}$ background is then further reduced by the $m_{\text{T2}}^{\text{b-jet}}$ requirement. The requirement on leading lepton p_{T} has little impact on the signal, but reduces the remaining Z/γ^*+jets background to a negligible level. The cut on m_{T2} ensures orthogonality with the analysis described in Ref. [20].

5.3 Event selection in the $t + \tilde{\chi}_1^0$ analysis

In addition to the preselection described in Section 5.1, events are required to have at least two jets, a leading jet with $p_{\text{T}} > 50$ GeV and $m_{\text{eff}} > 300$ GeV, where m_{eff} is the scalar sum of the $E_{\text{T}}^{\text{miss}}$, the transverse momenta of the two leptons and of the two most energetic jets in each event. The selected events are first divided into four (not mutually exclusive) categories, with the requirements in each category designed to target a different region of the $m(\tilde{t}_1) - m(\tilde{\chi}_1^0)$ plane:

- **(C1)** $E_{\text{T}}^{\text{miss}} > 50$ GeV: provide good sensitivity for $m(\tilde{t}_1)$ in the range 200-450 GeV;
- **(C2)** $E_{\text{T}}^{\text{miss}} > 80$ GeV: provide good sensitivity along the $m(\tilde{t}_1) = m(t) + m(\tilde{\chi}_1^0)$ line;
- **(C3)** $E_{\text{T}}^{\text{miss}} > 50$ GeV and leading lepton $p_{\text{T}} > 50$ GeV: provide good sensitivity for $m(\tilde{t}_1)$ in the range 400-500 GeV and > 500 GeV for high neutralino masses;
- **(C4)** $E_{\text{T}}^{\text{miss}} > 50$ GeV and leading lepton $p_{\text{T}} > 80$ GeV: provide good sensitivity for $m(\tilde{t}_1) > 500$ GeV.

Events are then further divided into those containing a same flavour lepton pair (SF) and those containing a different flavour lepton pair (DF). For SF events, only categories (C1) and (C3) are considered.

A BDTG discriminant is employed to further optimise the six regions described above. The following variables are given as input to the BDTG: $E_{\text{T}}^{\text{miss}}$, m_{ll}, m_{T2}, the azimuthal (ϕ) and polar (θ) angular difference between the two leptons, the angular difference in ϕ between $E_{\text{T}}^{\text{miss}}$ and the most energetic lepton, and between the most energetic jet and the leading lepton. Angular differences are taken in the range $[0, \pi]$ and, when computing the difference in θ between the two leptons, the momenta of the two

leptons are allowed to lie in opposite half-planes defined by the z axis. These variables are well modeled by the simulation and are effective in discriminating $t + \tilde{\chi}_1^0$ signal from SM background. Several BDTGs are trained using simulated background samples and various representative signal samples appropriate for each region C1 to C4. The resulting discriminants are bound between -1 and 1. The value of the cut on this discriminant for each of the regions is chosen to maximise sensitivity to the signal points considered, with the possible values of the BDTG threshold scanned in steps of 0.01. For each category (C1–C4) and signal sample a requirement on the corresponding BDTG optimising the discovery significance of that sample is derived. The resulting eleven BDTGs (seven for DF events, four for SF events) and BDTG requirements defining the regions (SR) are summarised in Table 2.

Table 2: Signal regions for the $t+\tilde{\chi}_1^0$ analysis. The first column gives the name of each SR, where DF and SF indicate different and same flavours, respectively. The second column gives the signal sample used to train the BDTG. The third column lists the selection requirements applied in addition to the BDTG requirement given in the fourth column.

	Training Sample $(m(\tilde{t}_1), m(\tilde{\chi}_1^0))$ [GeV]	Category	BDTG cut
$\mathrm{SR}_1^{\mathrm{DF}}$	(225,0)	C1	> -0.13
$\mathrm{SR}_2^{\mathrm{DF}}$	(225,25)	C1	> -0.33
$\mathrm{SR}_3^{\mathrm{DF}}$	(250,25)	C1	> -0.18
$\mathrm{SR}_4^{\mathrm{DF}}$	(300,50)	C1	> 0.19
$\mathrm{SR}_5^{\mathrm{DF}}$	(350,170)	C2	> -0.65
$\mathrm{SR}_6^{\mathrm{DF}}$	(500,250)	C3	> -0.32
$\mathrm{SR}_7^{\mathrm{DF}}$	(550,0)	C4	> -0.33
$\mathrm{SR}_1^{\mathrm{SF}}$	(225,25)	C1	> -0.66
$\mathrm{SR}_2^{\mathrm{SF}}$	(300,50)	C1	> -0.11
$\mathrm{SR}_3^{\mathrm{SF}}$	(300,100)	C1	> -0.77
$\mathrm{SR}_4^{\mathrm{SF}}$	(500,250)	C3	> -0.76

6 Background estimation

6.1 $b + \tilde{\chi}_1^{\pm}$ analysis

Top pair and single top (Wt channel) production contribute significantly to the background event yields in the SR for the $b + \tilde{\chi}_1^{\pm}$ analysis. Simulation shows that 49% of events in the SR are from top pair production and 37% are from Wt. The next most significant SM background contributions are those arising from misidentified (fake) leptons. The remainder of the background is composed of Z/γ^*+jets and WW. The contribution from other diboson processes, WZ and ZZ, is negligible.

The $t\bar{t}$ background is evaluated by defining a control region (CR) and using MC simulation to extrapolate the yield measured in the CR to that in the SR. The Wt contribution is estimated directly from MC simulation. A second CR is used to evaluate the $Z/\gamma^*(\rightarrow ee, \mu^+\mu^-)$+jets background. Details of the CR selections are listed below:

- **CRT**, defined by events with 1 b-jet, but passing all the SR selections on other variables. This region is populated by top quark pairs with a purity of 81%. When constructing $m_{\mathrm{T2}}^{\text{b-jet}}$ the highest p_{T} jet which is not a reconstructed b-jet is used with the single b-jet.

- **CRZ**, defined by SF events which pass all the selections of the SR, except that the two-lepton invariant mass is required to be between 81 GeV and 101 GeV and the leading lepton p_{T} must exceed 60 GeV. This region is populated by $Z/\gamma^*(\rightarrow ee, \mu^+\mu^-)$+jets with a purity of 92%.

With this approach, the ratio of events for each of the background sources in the CRs and SRs is taken from MC simulation, and the normalisation from data. Systematic uncertainties on MC simulation affect the ratio of the expected yields in the different regions and are taken into account to determine the uncertainty on the background prediction. The evaluation is performed by means of a likelihood fit, with the observed rates in the two CRs as constraints, and the normalisation terms for each of the two backgrounds in the signal region ($t\bar{t}$ and $Z/\gamma^*(\rightarrow ee, \mu^+\mu^-)$+jets) as free parameters. The systematic uncertainties are described by Gaussian nuisance parameters, which are not constrained by the fit. Each uncertainty source is described by a single nuisance parameter, and all correlations between background processes and selections are taken into account. The list of systematic uncertainties considered is described in the next section.

The fake lepton background consists of semi-leptonic $t\bar{t}$, s-channel and t-channel single top, W+jets and light- and heavy-flavour jet production. The contribution from this background is small (less than 10% of the total background). It is estimated from data with a method similar to that described in Refs. [79, 80]. Two types of lepton identification criteria are defined for this evaluation: "tight", corresponding to the full set of identification criteria described above, and "loose", corresponding to preselected electrons and muons. The method counts the number of observed events containing loose-loose, loose-tight, tight-loose and tight-tight lepton pairs in the selected region. The probability for real leptons passing the loose selection criteria to also pass the tight selection is measured using a $Z \rightarrow \ell\ell$ ($\ell = e, \mu$) sample. The equivalent probability for fake leptons is measured from multijet-enriched control samples. The number of events containing a contribution from one or two fake leptons is calculated from these probabilities.

The background composition of the two CRs is given in Table 3. Additional SM processes yielding two isolated leptons and $E_{\mathrm{T}}^{\mathrm{miss}}$ (WW, WZ, ZZ, $Z(\rightarrow \tau\tau)$+jets and $t\bar{t}+V$), which provide a sub-dominant contribution to the SR, are determined from MC simulation. In order to test the validity of the $t\bar{t}$ background estimate, and the combined estimate of the Wt and $t\bar{t}$ backgrounds, a validation region for the top background is defined:

- **VRT**, using events with leading lepton $p_{\mathrm{T}} > 60$ GeV, but passing all SR selections on other variables with the exception that the two-lepton invariant mass is required to be less than 81 GeV or greater than 101 GeV for SF events. This region is populated by top events (top-quark pairs and Wt single top) with a purity of 74%. A fraction of 50% of the top events are Wt single top, a similar percentage to that found in the SR.

Good agreement is seen between the observed and predicted event yield in VRT, as shown in Table 3.

Figure 1 shows the $m_{\mathrm{T2}}^{\text{b-jet}}$ distribution for events with 1 b-jet (using the highest p_{T} jet which is not a b-jet with the single b-jet in the calculation of $m_{\mathrm{T2}}^{\text{b-jet}}$), $m_{\mathrm{T2}} < 90$ GeV and leading lepton $p_{\mathrm{T}} < 60$ GeV. The events with $m_{\mathrm{T2}}^{\text{b-jet}} > 160$ GeV in the figure are those entering CRT. The data are in agreement with the background expectation across the distribution.

6.2 $t + \tilde{\chi}_1^0$ analysis

The dominant SM background processes are top quark pair production and diboson production. The Z/γ^*+jets contribution, relevant only for the SF channel, is suppressed by the BDTG requirement.

The contribution from $t\bar{t}$ in each SR is, as in the $b + \tilde{\chi}_1^{\pm}$ analysis, estimated by defining several CRs (one for each SR) and using MC simulation to extrapolate the yields measured in the CRs to the SRs.

Table 3: Background fit results for the two CRs and VRT region in the $b + \tilde{\chi}_1^{\pm}$ analysis. The nominal expectations from MC simulation are given for comparison for those backgrounds ($t\bar{t}$ and $Z/\gamma^*(\rightarrow ee, \mu^+\mu^-)$+jets production) which are normalised to data. Combined statistical and systematic uncertainties are given. Events with fake leptons are estimated with the data-driven technique described in Section 6.1.

channel	CRT	CRZ	VRT
Observed events	309	152	110
Total (constrained for CRT, CRZ) bkg events	309 ± 19	152 ± 12	110 ± 40
Fitted $t\bar{t}$ events	251 ± 25	$1.9^{+2.1}_{-1.9}$	38 ± 13
Fitted $Z\gamma^*(\rightarrow ee, \mu\mu)$+jets events	$0.8^{+1.1}_{-0.8}$	145 ± 13	20 ± 7
Expected $Z\gamma^*(\rightarrow \tau\tau)$+jets events	19 ± 13	0.14 ± 0.09	2.0 ± 0.4
Expected Wt events	18 ± 4	2.7 ± 1.9	34 ± 34
Expected WW events	3^{+4}_{-3}	$0.06^{+0.14}_{-0.06}$	1^{+3}_{-1}
Expected $t\bar{t} + V$ events	2.2 ± 0.7	1.4 ± 0.5	2.1 ± 0.7
Expected WZ, ZZ events	0.28 ± 0.15	$0.02^{+0.31}_{-0.02}$	$0.10^{+0.17}_{-0.10}$
Expected events with fake leptons	15 ± 6	$0.8^{+1.1}_{-0.8}$	9.0 ± 3.1
Fit input, expectation $t\bar{t}$	230 ± 50	$1.7^{+2.1}_{-1.7}$	35 ± 14
Fit input, expectation $Z\gamma^*(\rightarrow ee, \mu\mu)$+jets	$0.5^{+0.6}_{-0.5}$	90 ± 40	13.0 ± 2.6

All other backgrounds are small and evaluated using MC simulation. The CRs are defined in Table 4. In addition to the application of all non-BDTG SR cuts, the following selections are applied in the CRs: $m_{\mathrm{T2}} > 90$ GeV and, in SF events, m_{ll} must be less than 61 GeV or greater than 121 GeV. These requirements result in CRs with high $t\bar{t}$ purity ($> 90\%$) and kinematically close to the SRs, which are characterised by high m_{T2} values. CRs are chosen in mutually exclusive and largely more populated BDTG intervals with respect to SRs.

Table 4: The $t\bar{t}$ CRs defined for $t + \tilde{\chi}_1^0$ analysis. The name of each CR is given in the first column and these have a one to one correspondence with the equivalently named SR. The middle column lists all selection cuts made, whilst the final column gives the BDTG range.

Control region	Event variable cuts	BDTG range
$\mathrm{CR}_1^{\mathrm{DF}}$	C1, $m_{\mathrm{T2}} > 90$ GeV	> -1.00 and < -0.20
$\mathrm{CR}_2^{\mathrm{DF}}$	C1, $m_{\mathrm{T2}} > 90$ GeV	> -1.00 and < -0.50
$\mathrm{CR}_3^{\mathrm{DF}}$	C1, $m_{\mathrm{T2}} > 90$ GeV	> -1.00 and < -0.30
$\mathrm{CR}_4^{\mathrm{DF}}$	C1, $m_{\mathrm{T2}} > 90$ GeV	> -1.00 and < 0.00
$\mathrm{CR}_5^{\mathrm{DF}}$	C2, $m_{\mathrm{T2}} > 90$ GeV	> -1.00 and < -0.70
$\mathrm{CR}_6^{\mathrm{DF}}$	C3, $m_{\mathrm{T2}} > 90$ GeV	> -1.00 and < -0.50
$\mathrm{CR}_7^{\mathrm{DF}}$	C4, $m_{\mathrm{T2}} > 90$ GeV	> -1.00 and < -0.50
$\mathrm{CR}_1^{\mathrm{SF}}$	C1, $m_{\mathrm{T2}} > 90$ GeV, $m_{ll} < 61$ GeV or $m_{ll} > 121$ GeV	> -0.85 and < -0.75
$\mathrm{CR}_2^{\mathrm{SF}}$	C1, $m_{\mathrm{T2}} > 90$ GeV, $m_{ll} < 61$ GeV or $m_{ll} > 121$ GeV	> -0.85 and < -0.20
$\mathrm{CR}_3^{\mathrm{SF}}$	C1, $m_{\mathrm{T2}} > 90$ GeV, $m_{ll} < 61$ GeV or $m_{ll} > 121$ GeV	> -0.95 and < -0.80
$\mathrm{CR}_4^{\mathrm{SF}}$	C3, $m_{\mathrm{T2}} > 90$ GeV, $m_{ll} < 61$ GeV or $m_{ll} > 121$ GeV	> -0.98 and < -0.78

As an example, Figure 2 shows BDTG distributions for data and MC simulation in $\mathrm{CR}_4^{\mathrm{DF}}$ and $\mathrm{CR}_2^{\mathrm{SF}}$.

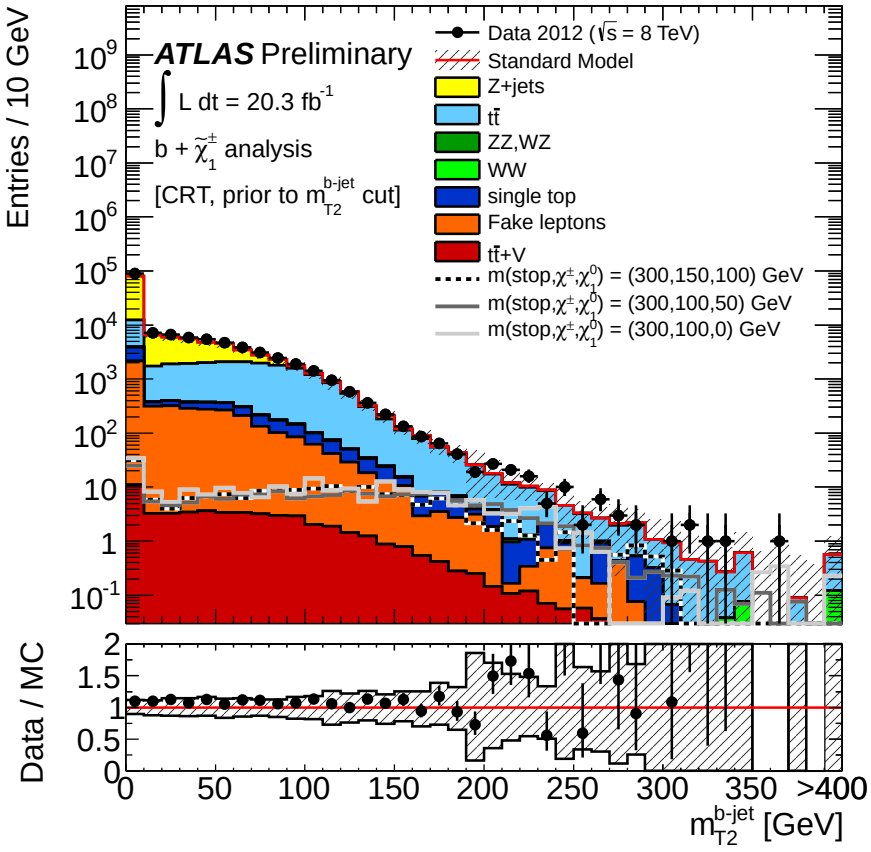

Figure 1: Distribution of $m_{\mathrm{T2}}^{\text{b-jet}}$ for events with 1 b-jet and all other CRT cuts, minus that on $m_{\mathrm{T2}}^{\text{b-jet}}$ itself. The contributions from all SM backgrounds are shown; the bands represent the total uncertainty. The component labelled "fake lepton" is estimated from data as described in the text; the other backgrounds are estimated from MC samples normalised to the luminosity of the data and their respective cross-sections. The expected distribution for three signal models is also shown: the dotted line corresponds to a model with m($\tilde{t}_1$)=300 GeV, m($\tilde{\chi}_1^{\pm}$)=150 GeV and m($\tilde{\chi}_1^0$)=100 GeV; the full line corresponds to a model with m($\tilde{t}_1$)=300 GeV, m($\tilde{\chi}_1^{\pm}$)=100 GeV and m($\tilde{\chi}_1^0$)=50 GeV; the dashed line to a model with m($\tilde{t}_1$) = 300 GeV, m($\tilde{\chi}_1^{\pm}$) = 100 GeV and m($\tilde{\chi}_1^0$)=1 GeV.

For each SR, the background is evaluated by means of a likelihood fit with the observed yields in each CR as constraints, and the normalisation of the $t\bar{t}$ background as a free parameter. This approach is the same as that of the $b + \tilde{\chi}_1^{\pm}$ analysis.

The expected background yields provided by the CR-only background fit are reported for each CR with their uncertainties in Tables 5 and 6 for the DF and SF CRs, respectively. The contributions of the fake leptons are estimated from data as described in Section 6.1.

7 Systematic Uncertainties

Various systematic uncertainties affecting the predicted background rates in the signal regions are considered. Such uncertainties are either used directly in the evaluation of the predicted background in the

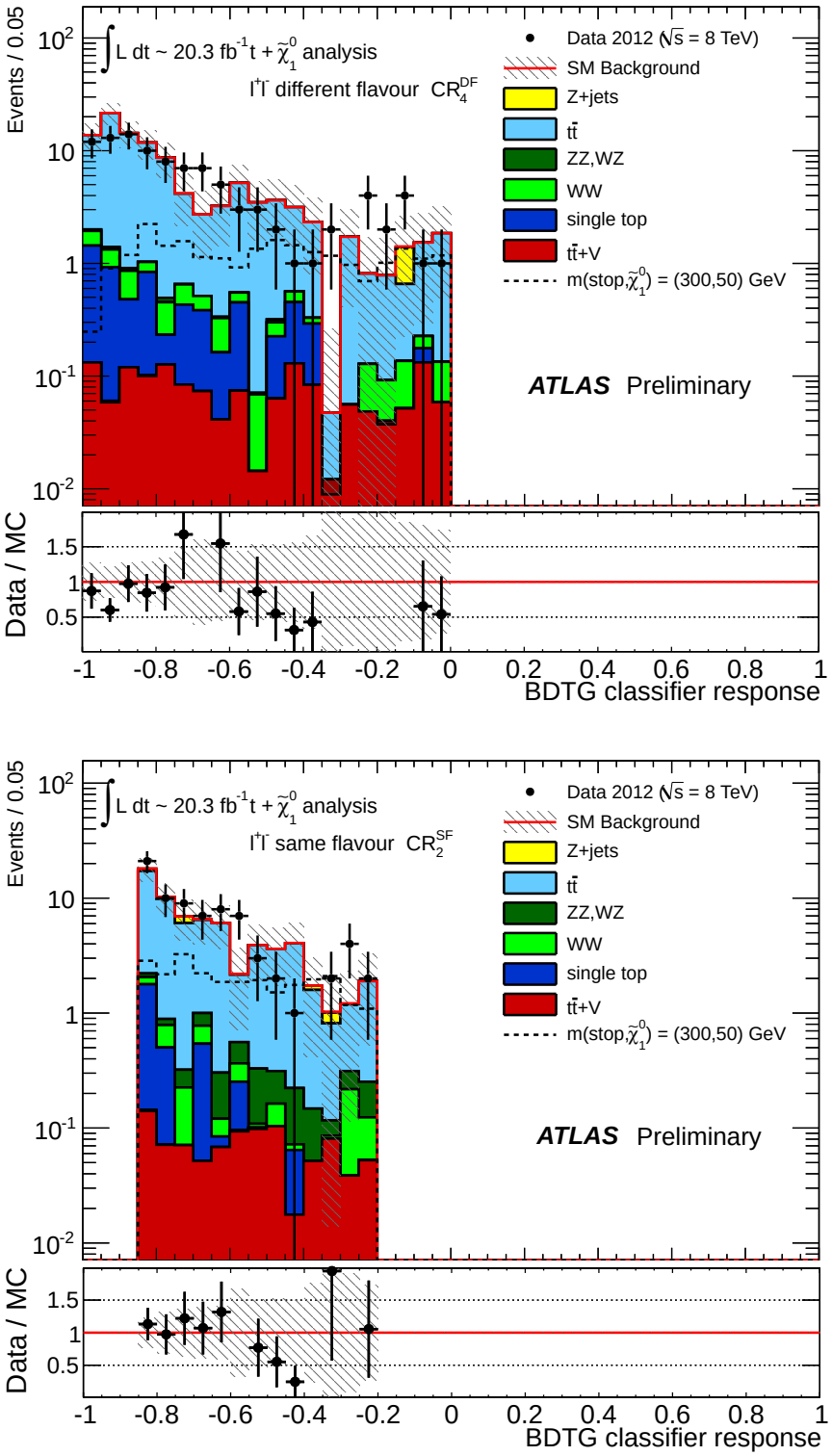

Figure 2: BDTG distributions of data and SM backgrounds for events in control regions CR_4^{DF} (top) and CR_2^{SF} (bottom). The contributions from all SM backgrounds are shown; the bands represent the uncertainty on the predicted yields due to the statistics of the simulated samples. The nominal backgrounds are estimated from simulated samples normalised to the luminosity of the data. The expected distribution for the signal point which was used to train the corresponding SR is also shown on each plot.

Table 5: Number of events and composition of the DF control regions for an integrated luminosity of 20.3 fb^{-1} in the $t + \tilde{\chi}_1^0$ analysis. Nominal MC simulation expectation is given for comparison for the background (top) which is normalised to data. Combined statistical and systematic uncertainties are given. Events with fake leptons are estimated with the data-driven technique described in Section 6.1.

channel	CR_1^{DF}	CR_2^{DF}	CR_3^{DF}	CR_4^{DF}	CR_5^{DF}	CR_6^{DF}	CR_7^{DF}
Observed events	407	398	395	415	358	396	245
Total (constrained) bkg events	407 ± 22	398 ± 21	395 ± 25	415 ± 21	358 ± 20	396 ± 40	245 ± 23
Fitted $t\bar{t}$ events	358 ± 26	350 ± 25	348 ± 28	366 ± 25	315 ± 24	350 ± 50	210 ± 25
Expected $t\bar{t} + V$ events	3.5 ± 1.6	2.9 ± 1.4	3.0 ± 1.5	3.1 ± 1.5	3.3 ± 1.5	3.5 ± 1.8	2.5 ± 1.3
Expected Wt events	19 ± 5	20 ± 5	19 ± 5	19 ± 5	15 ± 5	17 ± 5	15 ± 4
Expected WW events	$7.7^{+9.2}_{-7.7}$	7^{+9}_{-7}	7^{+8}_{-7}	7^{+9}_{-7}	6^{+8}_{-6}	8^{+9}_{-8}	6^{+7}_{-6}
Expected $ZW + ZZ$ events	0.9 ± 0.8	$0.8^{+0.9}_{-0.8}$	$0.8^{+0.9}_{-0.8}$	0.9 ± 0.8	$0.5^{+0.7}_{-0.5}$	0.9 ± 0.8	0.9 ± 0.7
Expected Z events	$0.4^{+0.9}_{-0.4}$	0.0	0.0	$0.4^{+1.0}_{-0.4}$	$0.3^{+0.9}_{-0.3}$	$0.4^{+0.9}_{-0.4}$	0.0
Expected events with fake leptons	17 ± 9	17 ± 9	17 ± 9	18 ± 9	16 ± 8	18 ± 9	11 ± 6
Fit input, expectation $t\bar{t}$	370 ± 50	360 ± 50	360 ± 50	370 ± 50	320 ± 50	350 ± 50	210 ± 40

Table 6: Number of events and composition of the SF control regions for an integrated luminosity of 20.3 fb^{-1} in the $t + \tilde{\chi}_1^0$ analysis. Nominal MC simulation expectation is given for comparison for the background (top) which is normalised to data. Combined statistical and systematic uncertainties are given. Events with fake leptons are estimated with the data-driven technique described in Section 6.1.

channel	CR_1^{SF}	CR_2^{SF}	CR_3^{SF}	CR_4^{SF}
Observed events	98	76	129	27
Total (constrained) bkg events	98 ± 11	76 ± 9	129 ± 12	27 ± 5
Fitted $t\bar{t}$ events	87 ± 14	63 ± 11	106 ± 14	20 ± 6
Expected $t\bar{t} + V$ events	0.91 ± 0.30	0.95 ± 0.30	1.4 ± 0.5	0.78 ± 0.31
Expected Wt events	1.9 ± 1.5	3.1 ± 1.9	4.2 ± 1.6	$0.7^{+0.9}_{-0.7}$
Expected WW events	$1.2^{+1.7}_{-1.2}$	$1.4^{+1.6}_{-1.4}$	$1.6^{+1.8}_{-1.6}$	$0.7^{+1.0}_{-0.7}$
Expected $ZW + ZZ$ events	1.2 ± 0.7	1.8 ± 0.9	1.8 ± 1.5	1.2 ± 0.7
Expected Z events	$1.8^{+7}_{-1.8}$	$1.7^{+6}_{-1.7}$	5 ± 5	$0.7^{+0.8}_{-0.7}$
Expected events with fake leptons	4.3 ± 2.2	3.2 ± 2.0	6.4 ± 2.9	2.2 ± 1.2
Fit input, expectation $t\bar{t}$	78 ± 12	58 ± 14	93 ± 14	19 ± 7

SR when this is derived using MC simulation, or to propagate the uncertainty to the predicted event yields in the SR when the fitting procedure is employed for the SM background estimates as described in Section 6 ($t\bar{t}$ and $Z/\gamma^* \to ee, \mu\mu$+jets events for the $b + \tilde{\chi}_1^\pm$ analysis, and $t\bar{t}$ for the $t + \tilde{\chi}_1^0$ analysis).

The experimental and theoretical systematic uncertainties are described in the following, and their size is given as a percentage of the total SM background yield.

Jet energy scale and resolution: the uncertainty on the jet energy scale (JES) has been derived using a combination of MC simulation and data [72] and varies as a function of the jet p_{T} and pseudorapidity. Additional systematic uncertainties arise from the dependence of the jet response on the number of interactions per bunch crossing and on the jet flavour. The components of the jet energy scale uncertainty are varied by $\pm 1\sigma$ in the MC simulation and propagated to the expected event yields. Uncertainties related to the jet energy resolution (JER) are obtained with an in situ measurement of the jet response asymmetry in dijet events [81]. Their impact on the event yields is estimated by applying an additional smearing to the jet transverse momenta in the MC simulation. The JES and JER variations applied to jets are propagated to the $E_{\mathrm{T}}^{\mathrm{miss}}$ calculation.

Calorimeter cluster energy scale, resolution and pile-up modelling: the uncertainties related to the contribution to $E_{\mathrm{T}}^{\mathrm{miss}}$ from the energy scale and resolution of the calorimeter cells not associated to electrons, muons or jets, as well as the uncertainty due to the modelling of pile-up have been evaluated as described in Ref. [77].

Fake-lepton background uncertainties: an uncertainty on the background estimate is assigned from the statistics of the control samples used to measure the probabilities to pass the tight selection, from the comparison of results obtained with these probabilities computed with alternative control samples, and from the number of events in the loose and tight event samples.

The uncertainties in the lepton reconstruction efficiency and in the trigger modelling have a negligible impact on the analysis. A $\pm 2.8\%$ uncertainty on the luminosity determination was measured using techniques similar to that described in Ref. [78], from a preliminary calibration of the luminosity scale derived from beam-separation scans performed in November 2012. It is included for all signal and background MC simulations.

The leading uncertainties on the estimate of the background in both analyses are those due to the modelling of the top backgrounds (both Wt and $t\bar{t}$, in the case of the $b + \tilde{\chi}_1^\pm$ analysis). In $b + \tilde{\chi}_1^\pm$ analysis, the predictions of `MC@NLO` are compared directly with `Powheg+Jimmy` to give an estimate of the uncertainty from the choice of generator, the difference in the yields obtained from `Powheg+Pythia` and `Powheg+Herwig` is taken as the systematic uncertainty on parton showering, and the predictions of dedicated `AcerMC` samples with different tunings are compared to give the uncertainty related to the amount of ISR/FSR. In the $t + \tilde{\chi}_1^0$ analysis, this procedure cannot be applied due to the limited number of simulated $t\bar{t}$ events from these MC samples in the SRs. In order to reduce the statistical fluctuation effects, the SF (DF) SR are each "enriched" by including in them the corresponding DF (SF) events. The predictions of the various $t\bar{t}$ generator pairings are then compared in these enriched regions. The differences in the predictions are then rescaled down to the number of events in the original SR. For the generator uncertainty, the statistical error on the `Powheg+Jimmy` yield is added in quadrature to the difference between the `Powheg+Jimmy` and `MC@NLO` yields.

At next-to-leading order, real contributions with an additional bottom quark in the final state lead to ambiguities in the conceptual distinction between the Wt process and top quark pair production. There are two possible methods for resolving this ambiguity [82]: diagram removal and diagram subtraction. `PowHeg` samples interfaced with `Pythia` are generated using using each of these two methods, with the difference between the yields of the two samples taken as the uncertainty due to this interference.

Other significant sources of uncertainty on the $b + \tilde{\chi}_1^\pm$ background estimate are the limited number of

Table 7: Leading systematic uncertainties in the $b + \tilde{\chi}_1^{\pm}$ analysis: the absolute variations in the predicted background yield are quoted. It should be noted that the individual uncertainties can be correlated. The rows labelled b-tagging B, C and mis-tag give the systematic uncertainties which arise from uncertainties in the b-tagging efficiencies which are measured separately for b-, c-, light and τ jets.

Signal channel	SR
Total systematic error	±5.71
Luminosity	±0.35
b-tagging B	±2.81
b-tagging C	±0.42
b-tagging mis-tag	±0.41
electron identification and reconstructing efficiency	±0.45
JER	±2.43
JES	±3.19
fake lepton uncertainties	±0.90
$E_{\mathrm{T}}^{\mathrm{miss}}$-scale	±0.29
WW generator	±0.34
Wt interference	±2.92
Wt cross-section	±0.62
$t\bar{t}$, Wt generator	±2.49
ISR,FSR	±1.33
$t\bar{t}$, Wt parton shower	±0.31
simulation sample size	±2.55
$t\bar{t}$ normalisation	±3.42

events in the CRs and MC simulation samples, and the uncertainty on the efficiency of the b-tagging. For the $t + \tilde{\chi}_1^0$ analysis the remaining important uncertainties relate to the diboson and Z+jets backgrounds. For dibosons, the uncertainties related to the generator are evaluated by comparing samples made with `Powheg` and `Sherpa`, while for Z+jets `Sherpa` and `Alpgen+Herwig` samples are compared.

A summary of the leading systematic uncertainties on the total expected background in the $b + \tilde{\chi}_1^{\pm}$ analysis is given in Table 7.

A summary of the leading systematic uncertainties on the total expected background in the $t + \tilde{\chi}_1^0$ analysis is given in Tables 8 and 9 for the DF and SF SRs, respectively.

Systematic uncertainties are also taken into account for expected signal yields. The uncertainty on the signal cross-sections is calculated with an envelope of cross-section predictions which is defined using the 68% confidence level (CL) ranges of the CTEQ [51] (including the α_S uncertainty) and MSTW [53] PDF sets, together with variations of the factorisation and renormalisation scales by factors of two or one half. The nominal cross-section value is taken to be the midpoint of the envelope and the uncertainty assigned is half the full width of the envelope, using the procedure described in Ref. [62]. The typical cross section uncertainty is 15% for the scalar top signal.

Table 8: Systematic uncertainties in the $t + \tilde{\chi}_1^0$ analysis for DF channels: the absolute variations in the predicted background yield are quoted. It should be noted that the individual uncertainties can be correlated.

Signal channel	SR_1^{DF}	SR_2^{DF}	SR_3^{DF}	SR_4^{DF}	SR_5^{DF}	SR_6^{DF}	SR_7^{DF}
Total systematic error	±1.98	±1.85	±4.62	±2.49	±0.75	±1.10	±1.44
$t\bar{t}$ ISR/FSR	±0.52	±0.61	±1.02	±0.80	±0.15	±0.75	±0.20
$t\bar{t}$ generator	±0.88	±0.69	±2.50	±1.35	±0.44	±0.45	±0.18
$t\bar{t}$ parton shower	±0.42	±0.82	±1.60	±0.37	±0.08	±0.54	±0.01
$t\bar{t}$ normalisation	±0.58	±0.33	±1.21	±0.64	±0.03	±0.00	±0.03
WW generator	±0.54	±0.05	±1.18	±0.91	±0.46	±0.24	±0.12
ZW+ZZ generator	±0.04	±0.05	±0.08	±0.09	±0.05	±0.05	±0.02
Z generator	±0.00	±0.00	±0.00	±0.00	±0.00	±0.00	±0.73
fake lepton uncertainties	±0.28	±0.10	±0.30	±0.27	±0.25	±0.25	±0.31
JES	±0.02	±0.14	±0.29	±0.47	±0.04	±0.06	±0.75
JER	±0.38	±1.05	±3.02	±0.87	±0.04	±0.03	±0.30
cluster energy scale	±0.73	±0.27	±1.20	±0.65	±0.03	±0.01	±0.07
cluster energy resolution	±0.07	±0.25	±0.08	±0.99	±0.04	±0.08	±0.07
pile-up	±1.22	±0.32	±1.64	±0.22	±0.17	±0.00	±0.14
sample size	±1.12	±0.80	±1.74	±1.20	±0.18	±0.09	±0.76

Table 9: Systematic uncertainties in the $t + \tilde{\chi}_1^0$ analysis for SF channels: the absolute variations in the predicted background yield are quoted. It should be noted that the individual uncertainties can be correlated.

Signal channel	SR_1^{SF}	SR_2^{SF}	SR_3^{SF}	SR_4^{SF}
Total systematic error	±4.49	±4.59	±1.43	±1.60
$t\bar{t}$ ISR/FSR	±0.62	±1.58	±0.41	±0.52
$t\bar{t}$ generator	±1.79	±2.10	±0.65	±0.68
$t\bar{t}$ parton shower	±3.00	±1.76	±0.06	±0.16
$t\bar{t}$ normalisation	±1.44	±1.90	±0.34	±0.28
WW generator	±0.09	±0.25	±0.04	±0.02
ZW+ZZ generator	±0.03	±0.33	±0.08	±0.64
Z generator	±0.00	±0.48	±0.22	±0.46
fake lepton uncertainties	±0.04	±0.73	±0.25	±0.05
JES	±0.07	±0.04	±0.02	±0.07
JER	±0.14	±2.84	±0.05	±0.77
cluster energy scale	±0.29	±0.32	±0.17	±0.06
cluster energy resolution	±0.43	±0.10	±0.01	±0.06
pile-up	±0.08	±0.67	±0.53	±0.09
sample size	±1.89	±1.40	±0.92	±0.59

8 Results

8.1 $b + \tilde{\chi}_1^{\pm}$ analysis

Figure 3 shows the distribution of the $m_{\mathrm{T2}}^{\text{b-jet}}$ variable after all SR cuts, except that on the $m_{\mathrm{T2}}^{\text{b-jet}}$ itself, after the background re-normalisation based on CRs. For illustration, the expected distributions for three signal models are also shown.

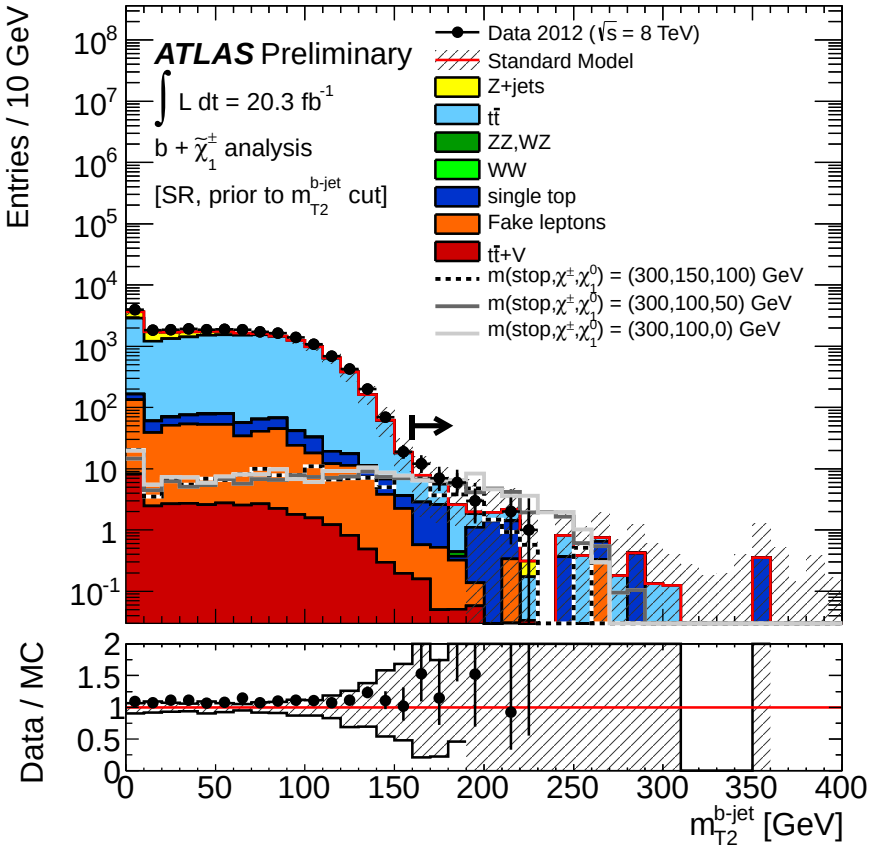

Figure 3: Distribution of $m_{\mathrm{T2}}^{\text{b-jet}}$ after all SR requirements, except that on $m_{\mathrm{T2}}^{\text{b-jet}}$ itself. The contributions from all SM backgrounds are shown; the bands represent the total uncertainty. The component labelled "fake lepton" is estimated from data as described in the text and the component labelled $t\bar{t}$ is shown re-normalised after the background fit; the other backgrounds are estimated from MC samples normalised to the luminosity of the data and their respective cross-sections. The expected distribution for three signal models is also shown: the dotted line corresponds to a model with m($\tilde{t}_1$)=300 GeV, m($\tilde{\chi}_1^{\pm}$)=150 GeV and m($\tilde{\chi}_1^0$)=100 GeV; the full line corresponds to a model with m($\tilde{t}_1$)=300 GeV, m($\tilde{\chi}_1^{\pm}$)=100 GeV and m($\tilde{\chi}_1^0$)=50 GeV; the dashed line to a model with m($\tilde{t}_1$) = 300 GeV, m($\tilde{\chi}_1^{\pm}$) = 100 GeV and m($\tilde{\chi}_1^0$)=1 GeV. The black line and arrow marks the start of the SR.

Table 10 shows the expected numbers of events in the SR for each background source and the observed numbers of events. No significant excess of events in data is observed. Limits at 95% CL are derived in Table 11 on the visible cross-section $\sigma_{\text{vis}} = \sigma \times \epsilon \times \mathcal{A}$, where σ is the production cross-section for the non-SM signal, $\mathcal{A}$ is the acceptance defined by the fraction of events passing the geometric and

kinematic selections at particle level, and ϵ is the detector reconstruction, identification and trigger efficiency. Limits are set using the CL_s likelihood ratio prescription as described in Ref. [83]. Systematic uncertainties are included in the likelihood function as nuisance parameters with a Gaussian probability density function. Uncertainties on the detector response, SM processes cross-sections, luminosity and MC samples statistics are taken into account. For each signal hypothesis, the fit of the $t\bar{t}$ and Z/γ^*+jets normalisation is re-done taking into account the signal contamination in the control regions. Signal contamination decreases with increasing stop mass and ranges from negligible to nearly 20%.

Table 10: Number of events and composition in SR for an integrated luminosity of 20.3 fb^{-1} at 8 TeV centre of mass energy, in the $b + \tilde{\chi}_1^{\pm}$ analysis. Nominal background expectations using MC samples normalised to their cross-sections and the luminosity of the data are given for comparison for those backgrounds ($t\bar{t}$ and Z/γ^*+jets production) which are normalised to data. Combined statistical and systematic uncertainties are given.

channel	SR
Observed events	31
Total (constrained to CRT, CRZ) expected background events	26 ± 6
Fitted $t\bar{t}$ events	14 ± 4
Fitted $Z\gamma^* \to ee, \mu\mu$+jets events	$0.23^{+0.30}_{-0.23}$
Expected $Z\gamma^* \to \tau\tau$+jets events	0.80 ± 0.21
Expected Wt events	9 ± 4
Expected WW events	$0.01^{+0.34}_{-0.01}$
Expected $t\bar{t} + V$ events	0.46 ± 0.16
Expected WZ, ZZ events	$0.08^{+0.09}_{-0.08}$
Expected events with fake leptons	1.8 ± 0.9
Fit input, expectation $t\bar{t}$	12 ± 5
Fit input, expectation $Z\gamma^* \to ee, \mu\mu$+jets	0.15 ± 0.15

Table 11: 95% CL upper limits and p-values for the $b + \tilde{\chi}_1^{\pm}$ analysis. The first column gives the 95% CL upper limit on the visible cross-section ($\langle\epsilon\sigma\rangle^{95}_{\rm obs}$). The second and third columns give the give the observed and expected upper limits on the number of signal events respectively. The fourth column gives the CL_B value, i.e. the confidence level observed for the background-only hypothesis, whilst the fifth column gives the discovery p-value ($p(s = 0)$).

Signal channel	$\langle\epsilon\sigma\rangle^{95}_{\rm obs}$[fb]	$S^{95}_{\rm obs}$ [events]	$S^{95}_{\rm exp}$ [events]	CL_B	$p(s = 0)$
SR	0.96	19.5	16^{+6}_{-5}	0.76	0.27

The results are used to derive limits on the masses of the $\tilde{\chi}_1^{\pm}$ and $\tilde{\chi}_1^0$ for a stop of 300 GeV mass which is pair-produced and decays with 100% branching ratio into a chargino and a b-quark. The resulting exclusion limit, after combination with the results in Ref. [20], is illustrated in Fig. 4, showing the complementarity between the analyses. For each signal point the p-values obtained using the SR (from either this $b + \tilde{\chi}_1^{\pm}$ analysis, or that in Ref. [20]) which gives the best expected p-value are taken.

Table 12: Number of events and composition of the DF signal regions for an integrated luminosity of 20.3 fb^{-1} in the $t+\tilde{\chi}_1^0$ analysis. Nominal background expectations using MC samples normalised to their cross-sections and the luminosity of the data are given for comparison for those backgrounds ($t\bar{t}$) which are normalised to data. Combined statistical and systematic uncertainties are given. Events with fake leptons are estimated with the data-driven technique described in Section 6.1

channel	SR_1^{DF}	SR_2^{DF}	SR_3^{DF}	SR_4^{DF}	SR_5^{DF}	SR_6^{DF}	SR_7^{DF}
Observed events	9	3	12	5	3	2	1
Total (constrained) bkg events	4.7 ± 2.0	2.5 ± 1.9	11 ± 5	6.3 ± 2.5	1.0 ± 0.8	$0.33^{+1.1}_{-0.33}$	1.6 ± 1.4
Fitted $t\bar{t}$ events	3.9 ± 1.9	2.2 ± 1.9	8 ± 4	4.1 ± 2.3	$0.2^{+1.0}_{-0.2}$	$0.0^{+1.0}_{-0.0}$	$0.1^{+0.6}_{-0.1}$
Expected $t\bar{t}+V$ events	0.49 ± 0.21	0.13 ± 0.06	1.0 ± 0.4	0.85 ± 0.35	0.41 ± 0.15	0.18 ± 0.07	0.24 ± 0.10
Expected Wt events	$0.00^{+0.09}_{-0.00}$	0.0	0.6 ± 0.6	0.4 ± 0.4	0.0	0.0	0.0
Expected WW events	$0.28^{+0.6}_{-0.28}$	$0.06^{+0.08}_{-0.06}$	$0.7^{+1.2}_{-0.7}$	$0.8^{+0.9}_{-0.8}$	$0.32^{+0.5}_{-0.32}$	$0.10^{+0.26}_{-0.10}$	0.49 ± 0.19
Expected $ZW+ZZ$ events	0.06 ± 0.06	$0.05^{+0.06}_{-0.05}$	0.09 ± 0.09	$0.09^{+0.11}_{-0.09}$	$0.05^{+0.06}_{-0.05}$	$0.05^{+0.06}_{-0.05}$	$0.02^{+0.03}_{-0.02}$
Expected Z events	0.0	0.0	0.0	0.0	0.0	0.0	$0.7^{+1.5}_{-0.7}$
Expected events with fake leptons	$0.00^{+0.28}_{-0.00}$	$0.03^{+0.10}_{-0.03}$	$0.00^{+0.30}_{-0.00}$	$0.00^{+0.27}_{-0.00}$	$0.00^{+0.25}_{-0.00}$	$0.00^{+0.25}_{-0.00}$	$0.00^{+0.31}_{-0.00}$
Fit input, expectation $t\bar{t}$	4.0 ± 2.2	2.3 ± 1.9	9 ± 5	4.2 ± 2.6	$0.2^{+0.6}_{-0.2}$	$0.0^{+1.1}_{-0.0}$	$0.1^{+0.6}_{-0.1}$

The overall reach in the 300 GeV stop plane is extended to lower neutralino-chargino mass differences. Chargino masses between 100 and 150 GeV are excluded for a 50 GeV neutralino and 300 GeV stop.

8.2 $t+\tilde{\chi}_1^0$ analysis

Figure 5 illustrates the BDTG distribution, after the background re-normalisation based on CRs and having applied all analysis selection cuts excluding the cut on the BDTG itself, for the DF and SF channels as obtained by training with the points $(m(\tilde{t}), m(\tilde{\chi}_1^0))$=(300,50) GeV and $(m(\tilde{t}),m(\tilde{\chi}_1^0))$=(300,100) GeV for the DF and SF channels, respectively. The two signal points used to train the BDTG in these SRs are indicated in the figure.

Tables 12 and 13 show the expected number of events in all DF and SF SRs, respectively, for each background source, together with the observed number of events. No significant excess of events in data is observed. Model independent limits are given in Table 14.

The exclusion limits at 95% CL in the $m(\tilde{t}) - m(\tilde{\chi}_1^0)$ plane are shown in Figure 6. The SR which gives the best expected p value is used at each point in the grid, and the results of the SF and DF channels are combined. Stop masses between 220 and 520 GeV are excluded for a massless neutralino. Neutralino masses below 140 GeV are excluded for stop masses around 430 GeV.

9 Conclusions

Two searches for a scalar partner of the top quark, one in which it decays into a b quark and a chargino, and another one in which it decays into a t quark and the lightest neutralino have been performed using data corresponding to 20.3 fb^{-1}of pp collisions at $\sqrt{s} = 8$ TeV, produced by the LHC and collected by the ATLAS detector. The numbers of observed events have been found to be consistent with the SM expectation for both analyses.

For a fixed 300 GeV mass of a stop decaying to a b-quark and a chargino, the results of this analysis extend the reach presented in Ref. [20] to lower chargino-neutralino mass differences. In particular, it increases the excluded region to include neutralino masses below 60 GeV for chargino masses up

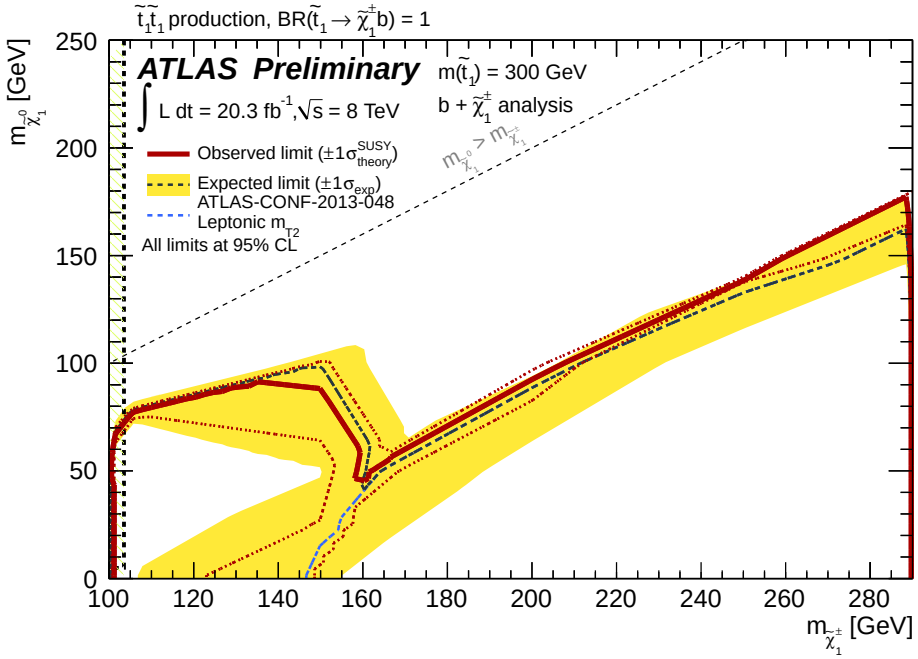

Figure 4: Exclusion limits at 95% CL from the analysis of 20.3 fb^{-1} of 8 TeV collision data on the masses of the chargino and the lightest neutralino, for a stop with a mass of 300 GeV and assuming BR($\tilde{t}_1 \to b + \tilde{\chi}_1^{\pm}$) = 1. The dark grey dashed line shows the expected limits, with the light yellow bands indicating the $\pm 1\sigma$ variation on the median expected limit due to the experimental and background-theory uncertainties. The observed nominal limit is indicated by a solid dark red line. The expected and observed limits do not include the effect of the theoretical uncertainties on the signal cross-section. The dark red dotted lines show the effect on the observed limit when applying a $\pm 1\sigma$ variation to the signal cross-section due to the scale and PDF uncertainties. The expected limit from the m_{T2} search in [20] is also reported. The limits are shown after a statistical combination with the results in [20] (picking the best expected signal region from either of the two analyses for each point). A band reaching up to the point with $m(\tilde{\chi}_1^{\pm}) = 160$ GeV and $m(\tilde{\chi}_1^0) = 50$ GeV is not excluded when the systematic errors are taken into account. The pale yellow shaded area (bounded by a vertical dashed line) illustrates the region with chargino masses less than 103.5 GeV excluded by LEP.

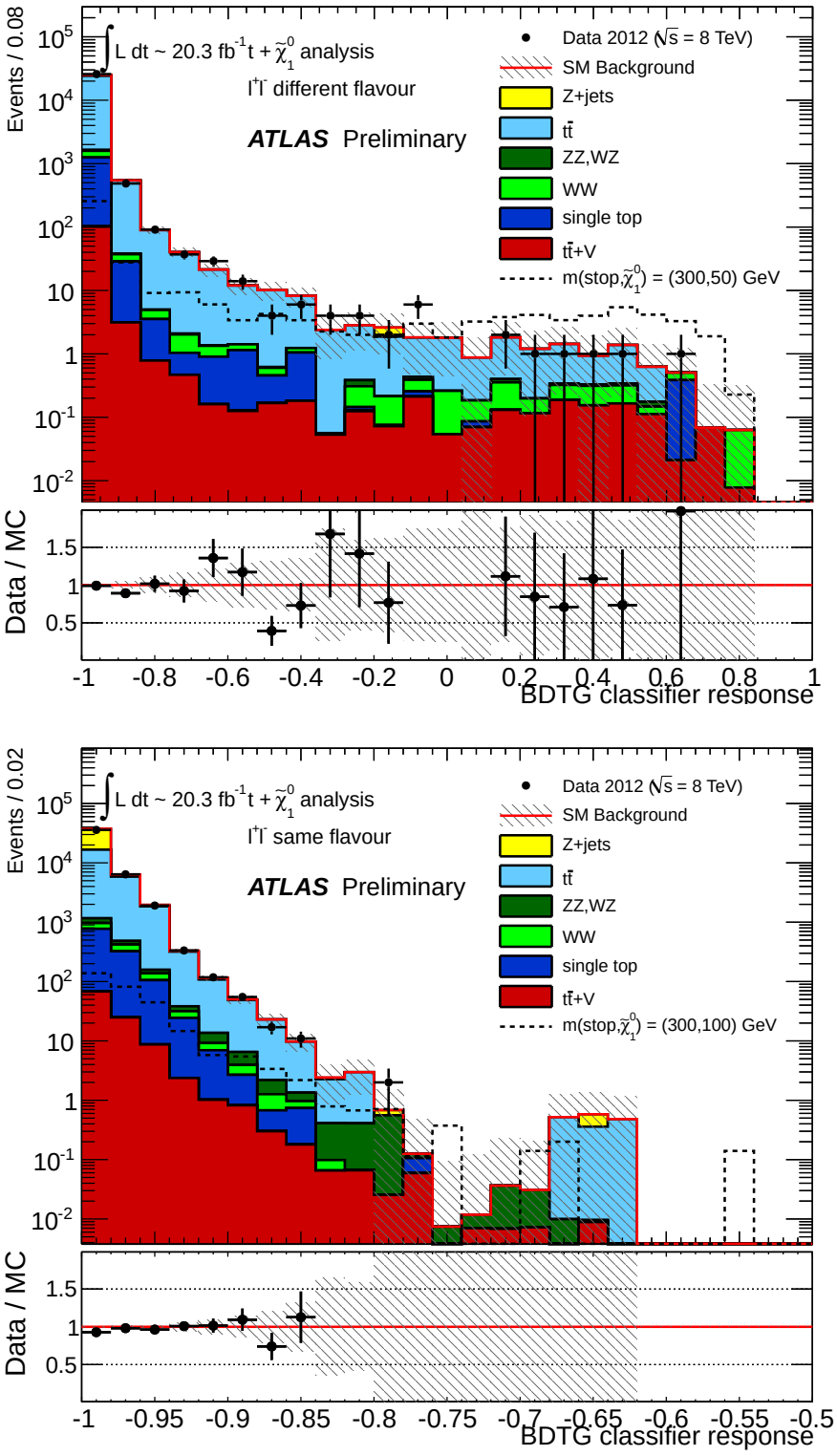

Figure 5: BDTG distribution in the $t + \tilde{\chi}_1^0$ analysis after all selection requirements, except the cut on the BDTG itself, after the background fit and for the DF (top) and SF (bottom) channels, as obtained from the trainings which used the point $(m(\tilde{t}), m(\tilde{\chi}_1^0))$=(300,50) GeV and $(m(\tilde{t}), m(\tilde{\chi}_1^0))$=(300,100) GeV, respectively. The reference signal points used in the training of each channel are also shown.

Table 13: Number of events and composition of the SF signal regions for an integrated luminosity of 20.3fb^{-1} in the $t + \tilde{\chi}_1^0$ analysis. Nominal background expectations using MC samples normalised to their cross-sections and the luminosity of the data are given for comparison for those backgrounds ($t\bar{t}$) which are normalised to data. Combined statistical and systematic uncertainties are given. Events with fake leptons are estimated with the data-driven technique described in Section 6.1

channel	SR_1^{SF}	SR_2^{SF}	SR_3^{SF}	SR_4^{SF}
Observed events	5	8	0	5
Total (constrained) bkg events	6 ± 4	9 ± 5	2.1 ± 1.4	2.5 ± 1.6
Fitted $t\bar{t}$ events	6 ± 4	5 ± 4	1.5 ± 1.4	$0.6^{+1.3}_{-0.6}$
Expected $t\bar{t} + V$ events	0.06 ± 0.03	0.49 ± 0.16	0.07 ± 0.04	0.19 ± 0.09
Expected Wt events	$0.00^{+0.08}_{-0.00}$	$0.02^{+0.24}_{-0.02}$	0.0	0.0
Expected WW events	$0.08^{+0.10}_{-0.08}$	$0.19^{+0.28}_{-0.19}$	$0.00^{+0.04}_{-0.00}$	$0.06^{+0.07}_{-0.06}$
Expected $ZW + ZZ$ events	$0.03^{+0.04}_{-0.03}$	2.0 ± 0.5	$0.08^{+0.10}_{-0.08}$	1.1 ± 0.7
Expected Z events	0.0	$0.5^{+0.6}_{-0.5}$	$0.2^{+0.4}_{-0.2}$	0.5 ± 0.5
Expected events with fake leptons	$0.00^{+0.04}_{-0.00}$	1.0 ± 0.7	0.25 ± 0.25	$0.00^{+0.05}_{-0.00}$
Fit input, expectation $t\bar{t}$	5 ± 4	5 ± 4	1.3 ± 1.1	$0.6^{+1.1}_{-0.6}$

Table 14: 95% CL upper limits and p-values for the $t + \tilde{\chi}_1^0$ analysis. The first column gives the 95% CL upper limits on the visible cross-sections ($\langle\epsilon\sigma\rangle^{95}_{\text{obs}}$). The second and third columns give the give the observed and expected upper limits on the number of signal events respectively. The fourth column give the CL_B values, i.e. the confidence levels observed for the background-only hypothesis, whilst the fifth column gives the discovery p-values ($p(s = 0)$). The numbers in parentheses represent the results obtained using asymptotic analytic expressions instead of toy Monte Carlo pseudo-experiments.

Signal channel	$\langle\epsilon\sigma\rangle^{95}_{\text{obs}}$[fb]	S^{95}_{obs} [events]	S^{95}_{exp} [events]	CL_B	$p(s = 0)$
SR_1^{DF}	0.57 (0.56)	11.7 (11.3)	$7.4^{+3.1}_{-1.9}$ ($7.2^{+3.5}_{-2.3}$)	0.91 (0.87)	0.08 (0.10)
SR_2^{DF}	0.33 (0.31)	6.6 (6.3)	$6.0^{+2.2}_{-1.2}$ ($5.9^{+2.7}_{-1.7}$)	0.64 (0.56)	0.37 (0.43)
SR_3^{DF}	0.61 (0.59)	12.4 (12.0)	$12.0^{+4.0}_{-2.8}$ ($11.7^{+4.5}_{-3.1}$)	0.57 (0.53)	0.35 (0.47)
SR_4^{DF}	0.34 (0.33)	6.8 (6.8)	$7.3^{+2.6}_{-1.8}$ ($7.2^{+3.3}_{-2.1}$)	0.42 (0.43)	0.43 (0.50)
SR_5^{DF}	0.33 (0.31)	6.6 (6.3)	$4.3^{+1.7}_{-0.6}$ ($4.0^{+2.4}_{-1.4}$)	0.91 (0.84)	0.08 (0.10)
SR_6^{DF}	0.28 (0.27)	5.7 (5.5)	$4.2^{+1.5}_{-0.3}$ ($4.2^{+2.3}_{-1.4}$)	0.83 (0.73)	0.10 (0.14)
SR_7^{DF}	0.21 (0.19)	4.3 (3.9)	$4.3^{+1.6}_{-1.1}$ ($4.2^{+2.3}_{-1.3}$)	0.48 (0.44)	0.42 (0.50)
SR_1^{SF}	0.45 (0.43)	9.0 (8.8)	$9.0^{+2.8}_{-1.6}$ ($8.9^{+3.2}_{-2.1}$)	0.53 (0.49)	0.48 (0.50)
SR_2^{SF}	0.48 (0.48)	9.8 (9.8)	$10.0^{+3.5}_{-2.2}$ ($10.0^{+3.8}_{-2.6}$)	0.47 (0.47)	0.45 (0.50)
SR_3^{SF}	0.15 (0.12)	3.0 (2.4)	$3.4^{+1.6}_{-0.4}$ ($3.4^{+2.2}_{-1.2}$)	0.20 (0.20)	0.36 (0.50)
SR_4^{SF}	0.43 (0.41)	8.7 (8.3)	$6.0^{+2.4}_{-1.1}$ ($5.8^{+3.0}_{-1.9}$)	0.87 (0.80)	0.13 (0.16)

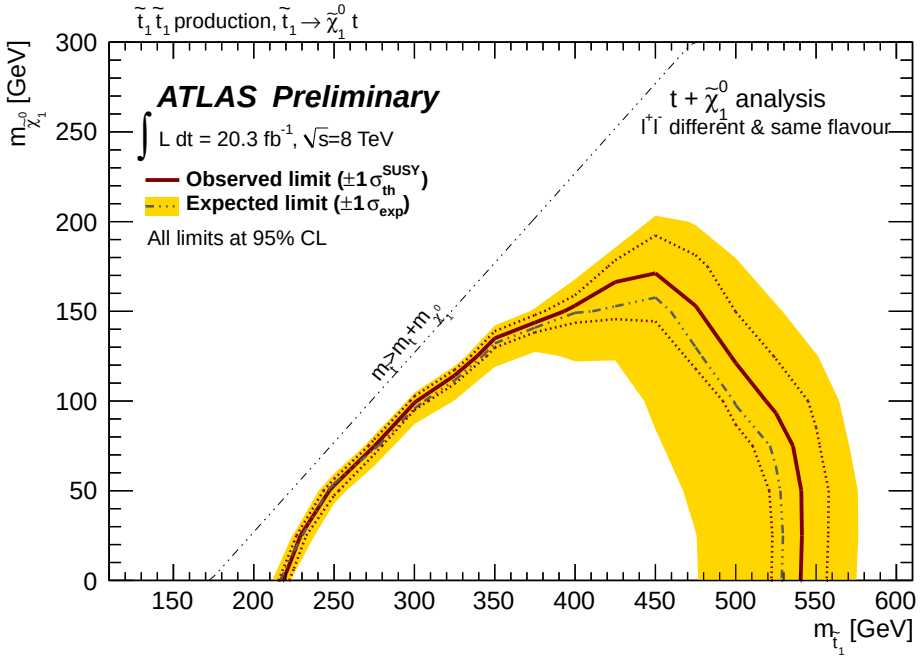

Figure 6: $t + \tilde{\chi}_1^0$ analysis: exclusion limits at 95% CL in the $m(\tilde{t}_1) - m(\tilde{\chi}_1^0)$ plane for the combination of the same flavour and different flavour channel from the analysis of 20.3 fb^{-1} of 8 TeV collision data. The dark grey dashed line shows the expected limits, with the light yellow bands indicating the $\pm1\sigma$ variation on the median expected limit due to the experimental and background-theory uncertainties. The observed nominal limit is indicated by a solid dark red line. The expected and observed limits do not include the effect of the theoretical uncertainties on the signal cross-section. The dark red dotted lines show the effect on the observed limit when applying a $\pm1\sigma$ variation to the signal cross-section due to the scale and PDF uncertainties.

to 140 GeV. A supersymmetric top squark of mass between ~220 GeV and ~520 GeV decaying with 100% BR to a t-quark and the lightest neutralino is excluded at 95% CL for a massless neutralino.

References

[1] S. Weinberg, Phys. Rev. **D13** (1976) 974–996.

[2] E. Gildener, Phys. Rev. **D14** (1976) 1667.

[3] S. Weinberg, Phys. Rev. **D19** (1979) 1277–1280.

[4] L. Susskind, Phys. Rev. **D20** (1979) 2619–2625.

[5] L. Evans and P. Bryant, JINST **3** (2008) S08001.

[6] H. Miyazawa, Prog. Theor. Phys. **36 (6)** (1966) 1266–1276.

[7] P. Ramond, Phys. Rev. **D3** (1971) 2415–2418.

[8] Y. Golfand and E. Likhtman, JETP Lett. **13** (1971) 323–326.

[9] A. Neveu and J. H. Schwarz, Nucl. Phys. **B31** (1971) 86–112.

[10] A. Neveu and J. H. Schwarz, Phys. Rev. **D4** (1971) 1109–1111.

[11] J. Gervais and B. Sakita, Nucl. Phys. **B34** (1971) 632–639.

[12] D. Volkov and V. Akulov, Phys. Lett. **B46** (1973) 109–110.

[13] J. Wess and B. Zumino, Phys. Lett. **B49** (1974) 52.

[14] J. Wess and B. Zumino, Nucl. Phys. **B70** (1974) 39–50.

[15] P. Fayet, Phys. Lett. **B64** (1976) 159.

[16] P. Fayet, Phys. Lett. **B69** (1977) 489.

[17] G. R. Farrar and P. Fayet, Phys. Lett. **B76** (1978) 575–579.

[18] P. Fayet, Phys. Lett. **B84** (1979) 416.

[19] S. Dimopoulos and H. Georgi, Nucl. Phys. **B193** (1981) 150.

[20] ATLAS Collaboration, ATLAS-CONF-2013-048. `https://cdsweb.cern.ch/record/1547564`.

[21] C. G. Lester and D. J. Summers, Phys. Lett. **B463** (1999) 99–103, `arXiv:hep-ph/9906349`.

[22] A. Barr, C. Lester, and P. Stephens, J. Phys. **G29** (2003) 2343–2363, `arXiv:hep-ph/0304226`.

[23] W. S. Cho, K. Choi, Y. G. Kim, and C. B. Park, JHEP **0802** (2008) 035, `arXiv:0711.4526 [hep-ph]`.

[24] M. Burns, K. Kong, K. T. Matchev, and M. Park, JHEP **0903** (2009) 143, `arXiv:0810.5576 [hep-ph]`.

[25] J. H. Friedman, tech. rep., March, 1999.

[26] A. Hoecker, P. Speckmayer, J. Stelzer, J. Therhaag, E. von Toerne, and H. Voss, CERN-OPEN-2007-007 (2009). arXiv:physics/0703039 [Data Analysis, Statistics and Probability].

[27] ATLAS Collaboration, Phys.Lett. **B720** (2013) 13–31, arXiv:1209.2102 [hep-ex].

[28] ATLAS Collaboration, Eur.Phys.J. **C72** (2012) 2237, arXiv:1208.4305 [hep-ex].

[29] ATLAS Collaboration, Phys.Rev.Lett. **109** (2012) 211802, arXiv:1208.1447 [hep-ex].

[30] ATLAS Collaboration, Phys.Rev.Lett. **109** (2012) 211803, arXiv:1208.2590 [hep-ex].

[31] ATLAS Collaboration, JHEP **1211** (2012) 094, arXiv:1209.4186 [hep-ex].

[32] ATLAS Collaboration, ATLAS-CONF-2013-037. https://cdsweb.cern.ch/record/1532431.

[33] ATLAS Collaboration, ATLAS-CONF-2013-024. https://cdsweb.cern.ch/record/1525880.

[34] ATLAS Collaboration, ATLAS-CONF-2012-171. https://cdsweb.cern.ch/record/1503233.

[35] CMS Collaboration, arXiv:1303.2985 [hep-ex].

[36] CMS Collaboration, CMS-PAS-SUS-13-003. https://cdsweb.cern.ch/record/1525539.

[37] CMS Collaboration, CMS-PAS-SUS-12-023. https://cdsweb.cern.ch/record/1494074.

[38] CMS Collaboration, CMS-PAS-SUS-11-030. https://cdsweb.cern.ch/record/1494575.

[39] ATLAS Collaboration, JINST **3** (2008) S08003.

[40] S. Frixione and B. R. Webber, JHEP **0206** (2002) 029, arXiv:hep-ph/0204244 [hep-ph].

[41] S. Frixione, E. Laenen, P. Motylinski, and B. R. Webber, JHEP **03** (2006) 092, arXiv:hep-ph/0512250.

[42] G. Corcella et al., JHEP **0101** (2001) 010, arXiv:hep-ph/0011363 [hep-ph].

[43] J. Butterworth, J. R. Forshaw, and M. Seymour, Z.Phys. **C72** (1996) 637–646, arXiv:hep-ph/9601371 [hep-ph].

[44] B. P. Kersevan and E. Richter-Was, arXiv:hep-ph/0405247 [hep-ph].

[45] S. Frixione, P. Nason, and C. Oleari, JHEP **0711** (2007) 070, arXiv:0709.2092 [hep-ph].

[46] T. Sjostrand, S. Mrenna, and P. Z. Skands, JHEP **0605** (2006) 026, arXiv:hep-ph/0603175 [hep-ph].

[47] J. Alwall, M. Herquet, F. Maltoni, O. Mattelaer, and T. Stelzer, JHEP **1106** (2011) 128, arXiv:1106.0522 [hep-ph].

[48] T. Gleisberg et al., JHEP **0902** (2009) 007, arXiv:0811.4622 [hep-ph].

[49] J. Pumplin et al., JHEP **0207** (2002) 012, arXiv:hep-ph/0201195 [hep-ph].

[50] M. L. Mangano, M. Moretti, F. Piccinini, R. Pittau, and A. D. Polosa, JHEP **0307** (2003) 001, arXiv:hep-ph/0206293 [hep-ph].

[51] P. M. Nadolsky et al., Phys. Rev. **D78** (2008) 013004, arXiv:0802.0007 [hep-ph].

[52] S. Catani et al., Phys.Rev.Lett. **103** (2009) 082001, arXiv:0903.2120 [hep-ph].

[53] A. D. Martin, W. J. Stirling, R. S. Thorne, and G. Watt, Eur. Phys. J. **C63** (2009) 189, arXiv:0901.0002 [hep-ph].

[54] M. Aliev et al., Comput.Phys.Commun. **182** (2011) 1034–1046, arXiv:1007.1327 [hep-ph].

[55] N. Kidonakis, Phys. Rev. **D82** (2010) 054018, arXiv:1005.4451 [hep-ph].

[56] T. Binoth, M. Ciccolini, N. Kauer, and M. Kramer, JHEP **0612** (2006) 046, arXiv:hep-ph/0611170 [hep-ph].

[57] A. Lazopoulos, T. McElmurry, K. Melnikov, and F. Petriello, Phys. Lett. **B666** (2008) 62–65, arXiv:0804.2220 [hep-ph].

[58] M.bahr and others, arxiv:0803.0883 [hep-ph] (2008).

[59] W. Beenakker, M. Kramer, T. Plehn, M. Spira, and P. M. Zerwas, Nucl. Phys. **B515** (1998) 3–14, hep-ph/9710451.

[60] W. Beenakker et al., JHEP **1008** (2010) 098, arXiv:1006.4771 [hep-ph].

[61] W. Beenakker et al., Int. J. Mod. Phys. **A26** (2011) 2637–2664, arXiv:1105.1110 [hep-ph].

[62] M. Kramer, A. Kulesza, R. van der Leeuw, M. Mangano, S. Padhi, T. Plehn, and X. Portell, arXiv:1206.2892.

[63] ATLAS Collaboration, ATL-PHYS-PUB-2010-014. http://cdsweb.cern.ch/record/1303025.

[64] ATLAS Collaboration, ATL-CONF-2010-031. http://cdsweb.cern.ch/record/1277665.

[65] GEANT4 Collaboration, S. Agostinelli et al., Nucl. Instrum. Meth. **A506** (2003) 250–303.

[66] ATLAS Collaboration, Eur. Phys. J. **C70** (2010) 823–874, arXiv:1005.4568 [physics.ins-det].

[67] E. Richter-Was, D. Froidevaux, and L. Poggioli,.

[68] M. Cacciari and G. P. Salam, Phys. Lett. **B641** (2006) 57–61, arXiv:hep-ph/0512210 [hep-ph].

[69] M. Cacciari, G. P. Salam, and G. Soyez, JHEP **0804** (2008) 063, arXiv:0802.1189 [hep-ph].

[70] T. Barillari et al., ATLAS-LARG-PUB-2009-001. https://cdsweb.cern.ch/record/1112035.

[71] ATLAS Collaboration, ATLAS-CONF-2013-004. https://cdsweb.cern.ch/record/1509552/.

[72] ATLAS Collaboration, Eur.Phys.J. **C73** (2013) 2304, arXiv:1112.6426 [hep-ex].

[73] ATLAS Collaboration, ATLAS-CONF-2011-102 (2011). http://cdsweb.cern.ch/record/1369219.

[74] ATLAS Collaboration, ATLAS-CONF-2012-097 (2012). http://cdsweb.cern.ch/record/1460443.

[75] ATLAS Collaboration, Eur. Phys. J. **C72** (2012) 1909, arXiv:1110.3174 [hep-ex].

[76] ATLAS Collaboration, ATLAS-CONF-2011-063.
https://cdsweb.cern.ch/record/1345743.

[77] ATLAS Collaboration, Eur. Phys. J. **C72** (2012) 1844, arXiv:1108.5602 [hep-ex].

[78] ATLAS Collaboration, arXiv:1302.4393 [hep-ex].

[79] ATLAS Collaboration, Eur. Phys. J. **C71** (2011) 1577, arXiv:1012.1792 [hep-ex].

[80] ATLAS Collaboration, Phys. Lett. **B707** (2012) 459–477, arXiv:1108.3699 [hep-ex].

[81] ATLAS Collaboration, ATL-CONF-2010-054. http://cdsweb.cern.ch/record/1281311.

[82] S. Frixione, E. Laenen, P. Motylinski, B. R. Webber, and C. D. White, JHEP **0807** (2008) 029, arXiv:0805.3067 [hep-ph].

[83] A. L. Read, J.Phys. **G28** (2002) 2693–2704.

A Appendix

Total events	100000
Cleaning cuts	93256.8
Trigger	55037.4
same flavour	
Two 10 GeV SF leptons	3384.9
Isolation	2629.3
$M_{ll} > 20$ GeV	2568.6
opposite sign	2538.1
Trigger lepton p_T requirements	2418.9
2 b jets	1035.1
$m_{\mathrm{T2}}^{\text{b-jet}} > 160$ GeV	145.6
$m_{\mathrm{T2}} < 90$ GeV	141.1
leading lepton p_T <90 GeV	72.0
different flavour	
Two 10 GeV DF leptons	5773.6
Isolation	4502.5
$M_{ll} > 20$ GeV	4369.8
opposite sign	4316.8
Trigger lepton p_T requirements	2247.5
2 b jets	859.3
$m_{\mathrm{T2}}^{\text{b-jet}} > 160$ GeV	121.5
$m_{\mathrm{T2}} < 90$ GeV	118.7
leading lepton $p_T < 90$ GeV	47.6

Table 15: Number of simulated events passing various stages of the selection in the in the $b+\tilde{\chi}_1^{\pm}$ analysis for a signal sample with $m(\tilde{t}_1)$=300 GeV, $m(\tilde{\chi}_1^{\pm})$ = 150 GeV and $m(\tilde{\chi}_1^0)$ = 50 GeV, and with the top squark decaying as $\tilde{t}_1 \rightarrow \tilde{\chi}_1^{\pm} b \rightarrow W^{(*)}\tilde{\chi}_1^0 b$ with unit probability. Event weights are applied to correct simulated events to data. "Isolation" includes the effects of tight ID for electrons and the isolation selection for both electrons and muons. "Cleaning cuts" refer to cuts applied to remove non-collision backgrounds and detector noise.

Signal sample: $(m(\tilde{t}_1), m(\tilde{\chi}_1^0))$	(225,0) GeV	(225,25) GeV	(250,25) GeV	(300,50) GeV	(300,100) GeV	(350,170) GeV	(500,250) GeV	(550,0) GeV
Total events	500000	500000	500000	500000	199000	430000	100000	100000
Electron Trigger and cleaning cuts	34067.0	33707.0	19467.7	7216.4	6893.4	2750.8	315.6	181.8
Muon Trigger and cleaning cuts	35658.2	35193.0	20073.2	7434.8	7146.1	2848.6	326.7	193.1
same flavour								
Two 10 GeV SF leptons	4191.8	4279.3	2388.6	861	841.1	339.1	37.4	18.7
Isolation	3071.5	3151.0	1747.1	628.5	617.9	252.1	27.3	14.3
opposite sign	2944.6	3019.8	1682.9	605.9	595.8	242.2	26.3	13.8
$m_{ll} > 20$ GeV	2871.6	2916.4	1638.7	588.8	577.3	232.9	25.8	13.6
leading lepton $p_T > 25$ GeV	2785.0	2813.3	1594.4	576.4	567.1	223.2	25.2	13.5
different flavour								
Two 10 GeV DF leptons	5954.4	4144.4	2359.1	872.3	862.9	351.4	38.4	19.1
Isolation	3175.6	3033.0	1728.9	641.6	637.0	254.8	26.6	14.2
opposite sign	3047.6	2909.8	1664.3	619.6	612.7	244.1	25.6	13.7
$m_{ll} > 20$ GeV	2947.9	2816.2	1615.0	604.9	593.8	233.5	24.9	13.5
leading lepton $p_T > 25$ GeV	2864.7	2734.5	1573.6	591.2	575.9	225.3	24.3	13.3

Table 16: Number of simulated events passing various stages of the selection in the in the $t + \tilde{\chi}_1^0$ analysis for all signal samples used to train the BDTG. Event weights are applied to correct simulated events to data. "Isolation" includes the effects of tight ID for electrons and the isolation selection for both electrons and muons. "Cleaning cuts" refer to cuts applied to remove non-collision backgrounds and detector noise.

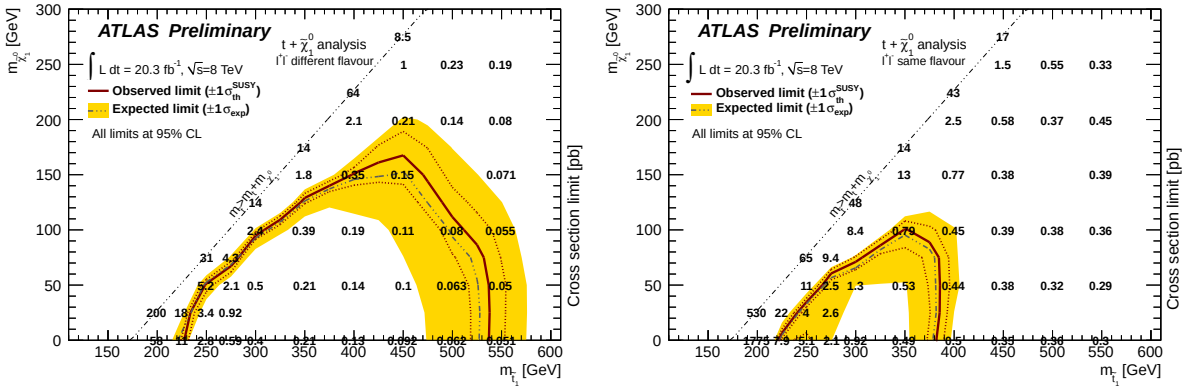

Figure 7: $t + \tilde{\chi}_1^0$ analysis: exclusion limits at 95% CL in the $m(\tilde{t}) - m(\tilde{\chi}_1^0)$ plane for the different flavour channel (left) and same flavour channel (right) from the analysis of 20.3 fb^{-1} of 8 TeV collision data. The dark grey dashed line shows the expected limits, with the light yellow bands indicating the $\pm1\sigma$ variation on the median expected limit due to the experimental and background-theory uncertainties. The observed nominal limit is indicated by a solid dark red line. The expected and observed limits do not include the effect of the theoretical uncertainties on the signal cross section. The dark red dotted lines show the effect on the observed limit when applying a $\pm1\sigma$ variation to the signal cross section due to the scale and PDF uncertainties. The overlaid numbers show the observed upper limit on the signal cross section, in pb, for each point of the grid.

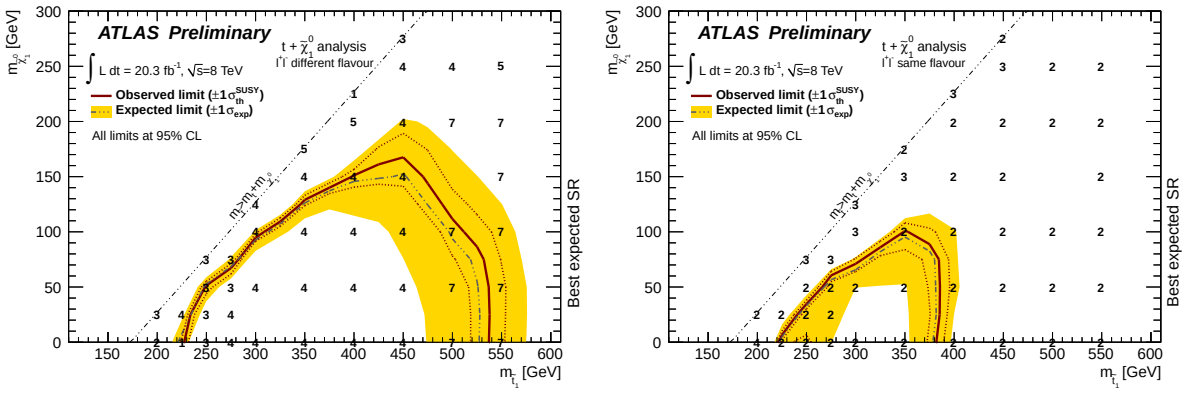

Figure 8: $t + \tilde{\chi}_1^0$ analysis: exclusion limits at 95% CL in the $m(\tilde{t}) - m(\tilde{\chi}_1^0)$ plane for the different flavour channel (left) and same flavour channel (right) from the analysis of 20.3 fb^{-1} of 8 TeV collision data. The dark grey dashed line shows the expected limits, with the light yellow bands indicating the $\pm1\sigma$ variation on the median expected limit due to the experimental and background-theory uncertainties. The observed nominal limit is indicated by a solid dark red line. The expected and observed limits do not include the effect of the theoretical uncertainties on the signal cross section. The dark red dotted lines show the effect on the observed limit when applying a $\pm1\sigma$ variation to the signal cross section due to the scale and PDF uncertainties. The best expected signal region is shown for each point.

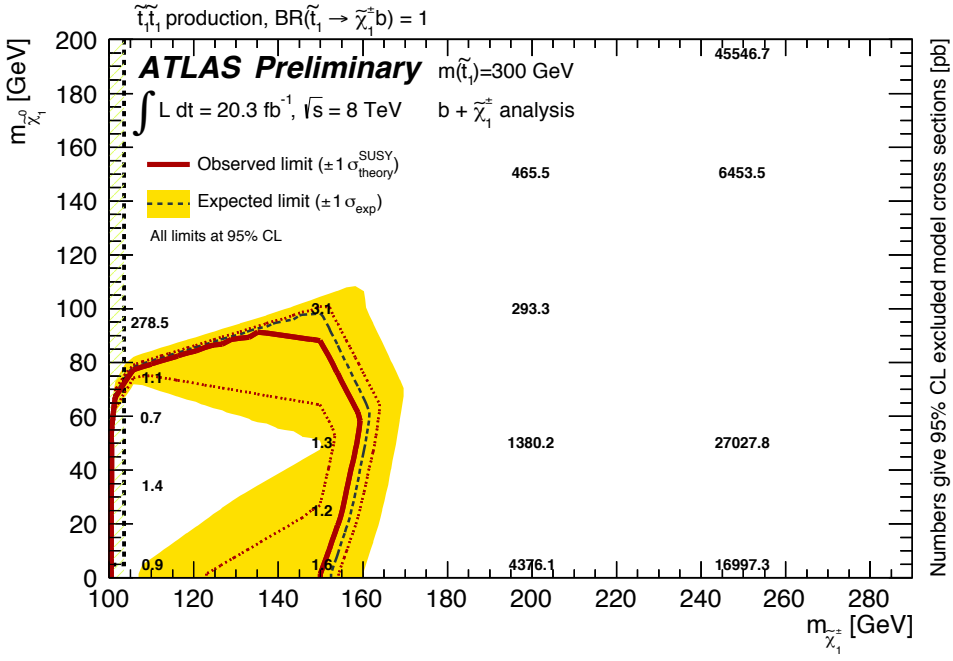

Figure 9: $b + \tilde{\chi}_1^{\pm}$ analysis: exclusion limits at 95% CL from the analysis of 20.3 fb^{-1} of 8 TeV collision data on the masses of the chargino and the lightest neutralino for a stop with a mass of 300 GeV assuming BR($\tilde{t}_1 \to b + \tilde{\chi}_1^{\pm}$) = 1. The dark grey dashed line shows the expected limits, with the light yellow bands indicating the $\pm 1\sigma$ variation on the median expected limit due to the experimental and background-theory uncertainties. The observed nominal limit is indicated by a solid dark red line. The expected and observed limits do not include the effect of the theoretical uncertainties on the signal cross section. The dark red dotted lines show the effect on the observed limit when applying a $\pm 1\sigma$ variation to the signal cross section due to the scale and PDF uncertainties. The overlaid numbers show the observed upper limit on the signal cross section, in pb.

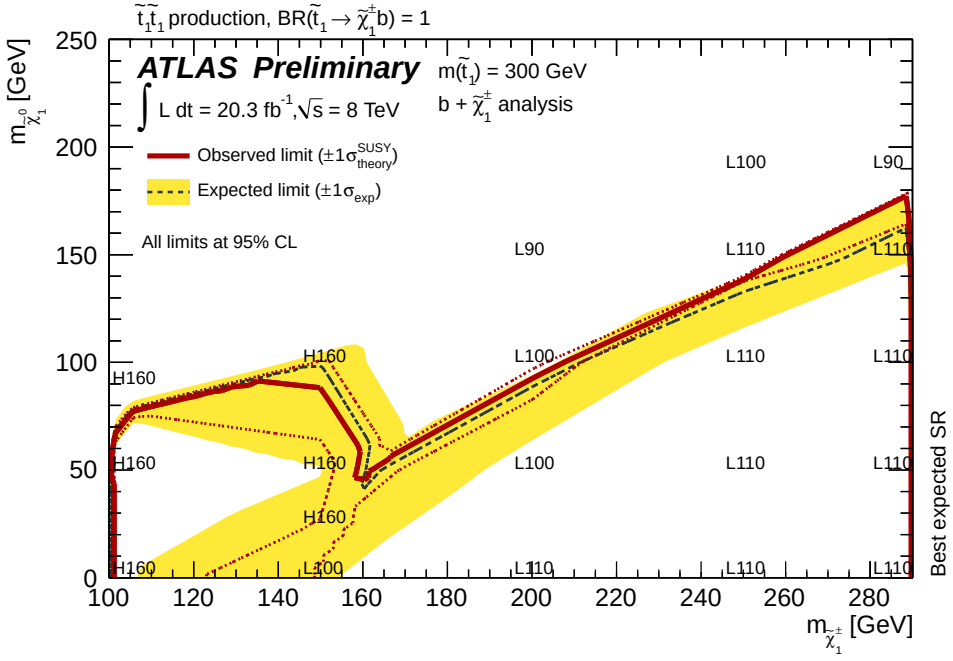

Figure 10: $b + \tilde{\chi}^0_{\pm}$ analysis: exclusion limits at 95% CL from the analysis of 20.3 fb^{-1} of 8 TeV collision data on the masses of the chargino and the lightest neutralino, for a stop with a mass of 300 GeV and assuming BR($\tilde{t}_1 \to b + \tilde{\chi}^{\pm}_1$) = 1. The dark grey dashed line shows the expected limits, with the light yellow bands indicating the $\pm1\sigma$ variation on the median expected limit due to the experimental and background-theory uncertainties. The observed nominal limit is indicated by a solid dark red line. The expected and observed limits do not include the effect of the theoretical uncertainties on the signal cross section. The dark red dotted lines show the effect on the observed limit when applying a $\pm1\sigma$ variation to the signal cross section due to the scale and PDF uncertainties. The expected limit from the m_{T2} search in Ref. [20] is also reported. The limits are shown before and after a statistical combination with the results in Ref. [20]. The best expected signal region is shown for each point ("H160"). The other labels denote the signal regions defined in Ref. [20].

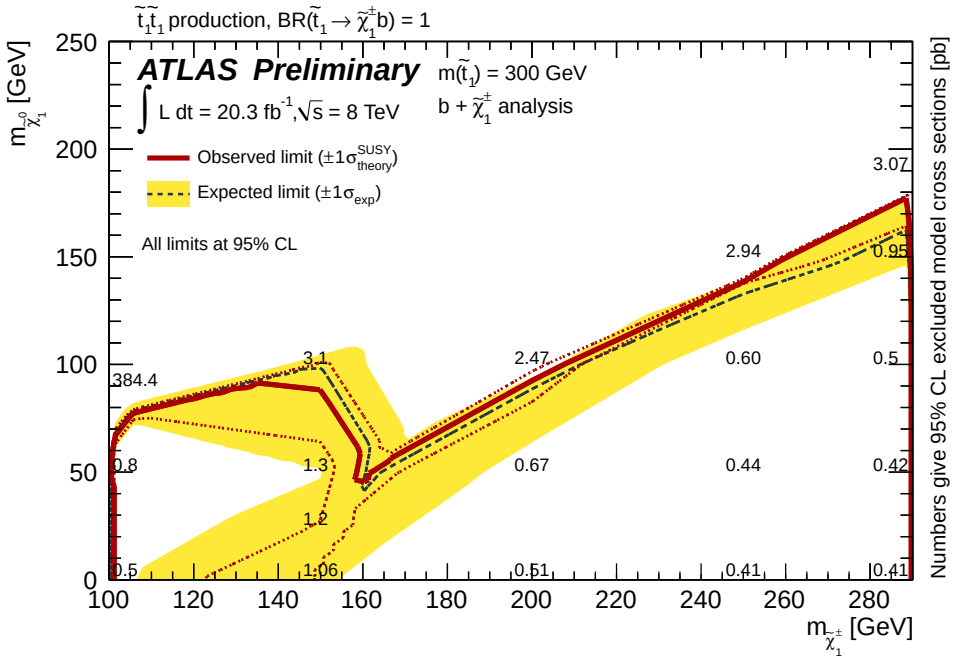

Figure 11: $b + \tilde{\chi}^0_{\pm}$ analysis: exclusion limits at 95% CL from the analysis of 20.3 fb^{-1} of 8 TeV collision data on the masses of the chargino and neutralino for a stop with a mass of 300 GeV assuming BR($\tilde{t}_1 \to b\tilde{\chi}^{\pm}_1$) = 1. The dark grey dashed line shows the expected limits, with the light yellow bands indicating the $\pm1\sigma$ variation on the median expected limit due to the experimental and background-theory uncertainties. The observed nominal limit is indicated by a solid dark red line. The expected and observed limits do not include the effect of the theoretical uncertainties on the signal cross section. The dark red dotted lines show the effect on the observed limit when applying a $\pm1\sigma$ variation to the signal cross section due to the scale and PDF uncertainties. The overlaid numbers show the observed upper limit on the signal cross section, in pb. The limits are shown after the statistical combination of the results with those in Ref. [20], using the best expected SR for each point.